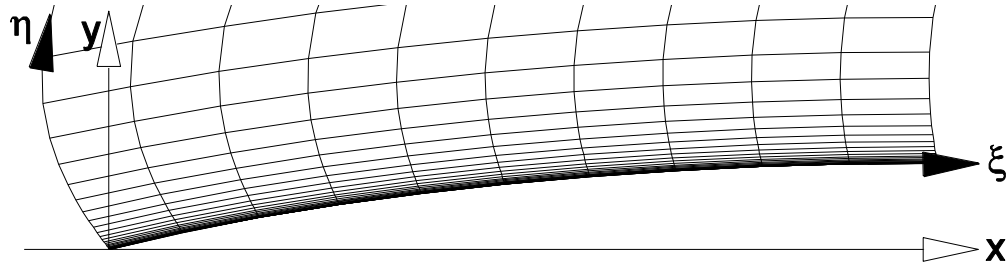# Chapter 17

Algorithms for the Navier-Stokes Equations - In 2-D Arbitrary Curvilinear Coordinates

17.1 The Navier-Stokes Equations in Arbitrary Curvilinear Coordinates

Figure 17.2 Mesh for a viscous flow at high Reynolds number along a curved surface

The transformation of equations from Cartesian coordinates to an arbitrary curvilinear coordinate system is discussed in Chapter 7.

$$\frac{\partial U}{\partial t}+\frac{\partial F}{\partial x}+\frac{\partial G}{\partial y}=0 \quad \Rightarrow \quad \frac{\partial U'}{\partial \tau}+\frac{\partial F'}{\partial \xi}+\frac{\partial G'}{\partial \eta}=0$$

where

$$U'=\frac{1}{d_{\xi\eta}}U, \quad d_{\xi\eta}=\frac{\partial \xi}{\partial x}\frac{\partial \eta}{\partial y}-\frac{\partial \xi}{\partial y}\frac{\partial \eta}{\partial x}$$

$$F'=\frac{1}{d_{\xi\eta}}\left(F\frac{\partial \xi}{\partial x}+G\frac{\partial \xi}{\partial y}+U\frac{\partial \xi}{\partial t}\right) \quad and \quad G'=\frac{1}{d_{\xi\eta}}\left(F\frac{\partial \eta}{\partial x}+G\frac{\partial \eta}{\partial y}+U\frac{\partial \eta}{\partial t}\right)$$

Using the identities given earlier in Sec.7.3,

$$U'=U\mathrm{V}, \quad F'=F\frac{\partial y}{\partial \eta}-G\frac{\partial x}{\partial \eta}+Uq_{\xi}, \quad G'=-F\frac{\partial y}{\partial \xi}+G\frac{\partial x}{\partial \xi}+Uq_{\eta}$$

where the metric volume term V and reference frame velocities q_{ξ} and q_{η} are given by

$$d_{xy}=\mathrm{V}=\frac{\partial x}{\partial \xi}\frac{\partial y}{\partial \eta}-\frac{\partial x}{\partial \eta}\frac{\partial y}{\partial \xi}, \quad q_{\xi}=\frac{\partial x}{\partial \eta}\frac{\partial y}{\partial \tau}-\frac{\partial y}{\partial \eta}\frac{\partial x}{\partial \tau}, \quad q_{\eta}=\frac{\partial y}{\partial \xi}\frac{\partial x}{\partial \tau}-\frac{\partial x}{\partial \xi}\frac{\partial y}{\partial \tau} \quad and \quad \tau=t$$

The metric volume term V, often called J to represent the Jacobian of the coordinate transformation, is here represented in non-italic face to distinguish it from the vector V given earlier containing the primitive flow variables as elements.

Assuming the arbitrary coordinate system is stationary, i.e., $q_\xi = 0$, $q_\eta = 0$ and volume V does not depend upon τ, the governing Navier-Stokes can be written as

$$\frac{\partial U}{\partial t} + \frac{1}{V}\frac{\partial F'}{\partial \xi} + \frac{1}{V}\frac{\partial G'}{\partial \eta} = 0 \tag{17.1}$$

$$\text{where } F' = F\frac{\partial y}{\partial \eta} - G\frac{\partial x}{\partial \eta} \quad and \quad G' = -F\frac{\partial y}{\partial \xi} + G\frac{\partial x}{\partial \xi}$$

Note that the above equation, written in an arbitrary coordinate system, still retains its Cartesian roots in that the state vector U is still written in terms of the Cartesian velocities u and v.

F' and G' represent rotated flux vectors, whose directions are orthogonal to the surfaces of constant ξ and η, respectively, though not necessarily orthogonal to each other.
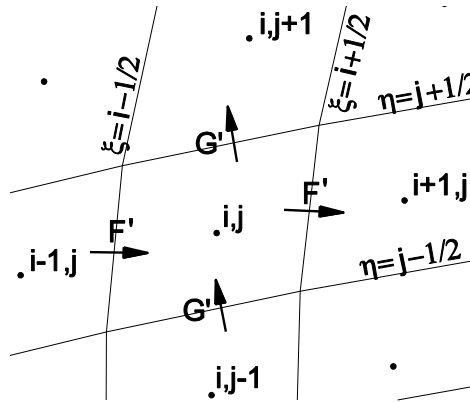
Figure 17.3 Computational coordinates induced from mesh point indices

17.2 Computational Coordinate System

Note that all spatial derivatives, of both the metric and flow variables, in the above formulation of the Navier-Stokes equations are now taken with respect to ξ and η only. These variables will now become the computational coordinates in which the governing equations will be discretized and solved. For structured body fitted meshes it is natural to use the indexing of the arrayed variables to induce the metric for the computational coordinates. Therefore, at grid point i, j $\xi = i$ and $\eta = j$ and at flux surfaces between grid points ξ and η will take on half integer values, i.e., $\xi = i + 1/2$ and $\eta = j + 1/2$. The distance between adjacent grid points is always $\Delta \xi = \Delta \eta = 1$ anywhere in the mesh. We will use this index induced metric herein.

The metric term V now has the dimensions of volume. In two dimensions we assume unit depth in the third dimension. However, care should be taken regarding the new flux terms F' and G' whose dimensions differ from those of F and G by surface area factors.

17.3 Euler Flux Terms and Rotated Jacobians

The flux vectors F' and G' contain both inviscid and viscous parts.

$$F' = F'_{Euler} + F'_{viscous} \quad and \quad G' = G'_{Euler} + G'_{viscous}$$

The Euler parts of these vectors can be represented as

$$F'_{Euler} = A'U \quad and \quad G'_{Euler} = B'U$$

where $A' = \dfrac{\partial y}{\partial n}A - \dfrac{\partial x}{\partial n}B, \quad B' = -\dfrac{\partial y}{\partial \xi}A + \dfrac{\partial x}{\partial \xi}B, \quad A = \dfrac{\partial F_{Euler}}{\partial U} \quad and \quad B = \dfrac{\partial G_{Euler}}{\partial U}$

Again, F' and G' represent rotated flux vectors. Similarly, A' and B' are rotated Jacobians. Again, caution should be maintained that they are dimensionally different from the Jacobians A and B in that they have an added factor of surface area. The rotated Jacobians can be shown equal to those given below, in which form they can be conveniently evaluated and diagonalized.

$$A' = S^{-1}R_{A'}^{-1}C_{A'}^{-1}\Lambda_{A'}C_{A'}R_{A'}S \quad and \quad B' = S^{-1}R_{B'}^{-1}C_{B'}^{-1}\Lambda_{B'}C_{B'}R_{B'}S$$

where S and S^{-1} are as given before in Section 9.6 and $C_{A'} = C_A$ and $C_{B'} = C_B$, which are also given in Section 9.6. $R_{A'}$ and $R_{B'}$ are rotation matrices with direction *cosine* and *sine* elements.

$$R_{A'} = \begin{bmatrix} 1 & 0 & 0 & 0 \\ 0 & \cos\alpha & \sin\alpha & 0 \\ 0 & -\sin\alpha & \cos\alpha & 0 \\ 0 & 0 & 0 & 1 \end{bmatrix} \quad and \quad R_{A'}^{-1} = \begin{bmatrix} 1 & 0 & 0 & 0 \\ 0 & \cos\alpha & -\sin\alpha & 0 \\ 0 & \sin\alpha & \cos\alpha & 0 \\ 0 & 0 & 0 & 1 \end{bmatrix}$$

where $\quad \cos\alpha = \dfrac{\dfrac{\partial y}{\partial \eta}}{\sqrt{\left(\dfrac{\partial x}{\partial \eta}\right)^2 + \left(\dfrac{\partial y}{\partial \eta}\right)^2}} \quad$ and $\quad \sin\alpha = \dfrac{-\dfrac{\partial x}{\partial \eta}}{\sqrt{\left(\dfrac{\partial x}{\partial \eta}\right)^2 + \left(\dfrac{\partial y}{\partial \eta}\right)^2}}$,

$$R_{B'} = \begin{bmatrix} 1 & 0 & 0 & 0 \\ 0 & \cos\beta & -\sin\beta & 0 \\ 0 & \sin\beta & \cos\beta & 0 \\ 0 & 0 & 0 & 1 \end{bmatrix} \quad \text{and} \quad R_{B'}^{-1} = \begin{bmatrix} 1 & 0 & 0 & 0 \\ 0 & \cos\beta & \sin\beta & 0 \\ 0 & -\sin\beta & \cos\beta & 0 \\ 0 & 0 & 0 & 1 \end{bmatrix}$$

$$\text{where} \quad \cos\beta = \frac{\dfrac{\partial x}{\partial \xi}}{\sqrt{\left(\dfrac{\partial x}{\partial \xi}\right)^2 + \left(\dfrac{\partial y}{\partial \xi}\right)^2}} \quad \text{and} \quad \sin\beta = \frac{-\dfrac{\partial y}{\partial \xi}}{\sqrt{\left(\dfrac{\partial x}{\partial \xi}\right)^2 + \left(\dfrac{\partial y}{\partial \xi}\right)^2}}$$

The diagonal matrices $\Lambda_{A'}$ and $\Lambda_{B'}$ are given by

$$\Lambda_{A'} = d_{A'} \begin{bmatrix} u' & 0 & 0 & 0 \\ 0 & u'+c & 0 & 0 \\ 0 & 0 & u' & 0 \\ 0 & 0 & 0 & u'-c \end{bmatrix}, \quad \Lambda_{B'} = d_{B'} \begin{bmatrix} v' & 0 & 0 & 0 \\ 0 & v' & 0 & 0 \\ 0 & 0 & v'+c & 0 \\ 0 & 0 & 0 & v'-c \end{bmatrix}$$

$$\text{where} \quad d_{A'} = \sqrt{\left(\frac{\partial x}{\partial \eta}\right)^2 + \left(\frac{\partial y}{\partial \eta}\right)^2}, \quad d_{B'} = \sqrt{\left(\frac{\partial x}{\partial \xi}\right)^2 + \left(\frac{\partial y}{\partial \xi}\right)^2}$$

$$u' = \cos\alpha\, u + \sin\alpha\, v \quad \text{and} \quad v' = \sin\beta\, u + \cos\beta\, v$$

The additional factor of surface area is evident in the definitions of the diagonal matrices $\Lambda_{A'}$ and $\Lambda_{B'}$ by comparison with those defined previously in Section 9.6.

17.4 Viscous Flux Terms
The viscous flux terms are

$$F'_{viscous} = F_{viscous}\frac{\partial y}{\partial \eta} - G_{viscous}\frac{\partial x}{\partial \eta} \quad \text{and} \quad G'_{viscous} = -F_{viscous}\frac{\partial y}{\partial \xi} + G_{viscous}\frac{\partial x}{\partial \xi} \tag{17.2}$$

$$F_{viscous} = \begin{bmatrix} 0 \\ -\tau_{xx} \\ -\tau_{xy} \\ -\tau_{xx}u - \tau_{xy}v - k\dfrac{\partial T}{\partial x} \end{bmatrix} = \begin{bmatrix} 0 \\ -\lambda\left(\dfrac{\partial u}{\partial x} + \dfrac{\partial v}{\partial y}\right) - 2\mu\dfrac{\partial u}{\partial x} \\ -\mu\left(\dfrac{\partial u}{\partial y} + \dfrac{\partial v}{\partial x}\right) \\ -\tau_{xx}u - \tau_{xy}v - k\dfrac{\partial T}{\partial x} \end{bmatrix}$$

$$\text{or} \quad F_{viscous} = -M_{xx}\frac{\partial V}{\partial x} - M_{xy}\frac{\partial V}{\partial y} \quad \text{with} \quad V = \begin{bmatrix} \rho \\ u \\ v \\ T \end{bmatrix}$$

$$\text{where} \quad M_{xx} = \begin{bmatrix} 0 & 0 & 0 & 0 \\ 0 & \lambda + 2\mu & 0 & 0 \\ 0 & 0 & \mu & 0 \\ 0 & u(\lambda + 2\mu) & v\mu & k \end{bmatrix} \quad \text{and} \quad M_{xy} = \begin{bmatrix} 0 & 0 & 0 & 0 \\ 0 & 0 & \lambda & 0 \\ 0 & \mu & 0 & 0 \\ 0 & v\mu & u\lambda & 0 \end{bmatrix}$$

Similarly,

$$G_{viscous} = \begin{bmatrix} 0 \\ -\tau_{xy} \\ -\tau_{yy} \\ -\tau_{xy}u - \tau_{yy}v - k\dfrac{\partial T}{\partial y} \end{bmatrix} = \begin{bmatrix} 0 \\ -\mu\left(\dfrac{\partial u}{\partial y} + \dfrac{\partial v}{\partial x}\right) \\ -\lambda\left(\dfrac{\partial u}{\partial x} + \dfrac{\partial v}{\partial y}\right) - 2\mu\dfrac{\partial v}{\partial y} \\ -\tau_{xy}u - \tau_{yy}v - k\dfrac{\partial T}{\partial y} \end{bmatrix}$$

$$\text{or} \quad G_{viscous} = -M_{yx}\frac{\partial V}{\partial x} - M_{yy}\frac{\partial V}{\partial y}$$

$$\text{where} \quad M_{yx} = \begin{bmatrix} 0 & 0 & 0 & 0 \\ 0 & 0 & \mu & 0 \\ 0 & \lambda & 0 & 0 \\ 0 & v\lambda & u\mu & 0 \end{bmatrix} \quad \text{and} \quad M_{yy} = \begin{bmatrix} 0 & 0 & 0 & 0 \\ 0 & \mu & 0 & 0 \\ 0 & 0 & \lambda + 2\mu & 0 \\ 0 & u\mu & v(\lambda + 2\mu) & k \end{bmatrix}$$

The viscous flux terms $F_{viscous}$ and $G_{viscous}$ are defined in terms of derivatives with respect to x and y, which can not be directly obtained in the computational coordinate system. They can be

obtained, however, on the $\xi - \eta$ coordinate system through use of the transformation given in Sec.7.2, which is rewritten as follows.

$$\begin{bmatrix} \dfrac{\partial}{\partial x} \\ \dfrac{\partial}{\partial y} \end{bmatrix} = \frac{1}{d_{xy}} \begin{bmatrix} \dfrac{\partial y}{\partial \eta} & -\dfrac{\partial y}{\partial \xi} \\ -\dfrac{\partial x}{\partial \eta} & \dfrac{\partial x}{\partial \xi} \end{bmatrix} \begin{bmatrix} \dfrac{\partial}{\partial \xi} \\ \dfrac{\partial}{\partial \eta} \end{bmatrix} \quad \text{with} \quad d_{xy} = \frac{\partial x}{\partial \xi} \frac{\partial y}{\partial \eta} - \frac{\partial x}{\partial \eta} \frac{\partial y}{\partial \xi}$$

The viscous flux vectors then can be written

$$F_{viscous} = -\frac{1}{d_{xy}} \left[\frac{\partial y}{\partial \eta} M_{xx} - \frac{\partial x}{\partial \eta} M_{xy} \right] \frac{\partial V}{\partial \xi} - \frac{1}{d_{xy}} \left[-\frac{\partial y}{\partial \xi} M_{xx} + \frac{\partial x}{\partial \xi} M_{xy} \right] \frac{\partial V}{\partial \eta}$$

and

$$G_{viscous} = -\frac{1}{d_{xy}} \left[\frac{\partial y}{\partial \eta} M_{yx} - \frac{\partial x}{\partial \eta} M_{yy} \right] \frac{\partial V}{\partial \xi} - \frac{1}{d_{xy}} \left[-\frac{\partial y}{\partial \xi} M_{yx} + \frac{\partial x}{\partial \xi} M_{yy} \right] \frac{\partial V}{\partial \eta}$$

Finally, Equation (17.2) becomes

$$F'_{viscous} = -M_{\xi\xi} \frac{\partial V}{\partial \xi} - M_{\xi\eta} \frac{\partial V}{\partial \eta} \quad \text{and} \quad G'_{viscous} = -M_{\eta\xi} \frac{\partial V}{\partial \xi} - M_{\eta\eta} \frac{\partial V}{\partial \eta} \tag{17.3}$$

where

$$M_{\xi\xi} = \frac{1}{d_{xy}} \left(\frac{\partial y}{\partial \eta} \frac{\partial y}{\partial \eta} M_{xx} - \frac{\partial x}{\partial \eta} \frac{\partial y}{\partial \eta} M_{xy} - \frac{\partial y}{\partial \eta} \frac{\partial x}{\partial \eta} M_{yx} + \frac{\partial x}{\partial \eta} \frac{\partial x}{\partial \eta} M_{yy} \right)$$

$$M_{\xi\eta} = \frac{1}{d_{xy}} \left(-\frac{\partial y}{\partial \xi} \frac{\partial y}{\partial \eta} M_{xx} + \frac{\partial x}{\partial \xi} \frac{\partial y}{\partial \eta} M_{xy} + \frac{\partial y}{\partial \xi} \frac{\partial x}{\partial \eta} M_{yx} - \frac{\partial x}{\partial \xi} \frac{\partial x}{\partial \eta} M_{yy} \right)$$

$$M_{\eta\xi} = \frac{1}{d_{xy}} \left(-\frac{\partial y}{\partial \eta} \frac{\partial y}{\partial \xi} M_{xx} + \frac{\partial x}{\partial \eta} \frac{\partial y}{\partial \xi} M_{xy} + \frac{\partial y}{\partial \eta} \frac{\partial x}{\partial \xi} M_{yx} - \frac{\partial x}{\partial \eta} \frac{\partial x}{\partial \xi} M_{yy} \right)$$

$$M_{\eta\eta} = \frac{1}{d_{xy}} \left(\frac{\partial y}{\partial \xi} \frac{\partial y}{\partial \xi} M_{xx} - \frac{\partial x}{\partial \xi} \frac{\partial y}{\partial \xi} M_{xy} - \frac{\partial y}{\partial \xi} \frac{\partial x}{\partial \xi} M_{yx} + \frac{\partial x}{\partial \xi} \frac{\partial x}{\partial \xi} M_{yy} \right)$$

17.5 The Navier-Stokes Flux Vectors

For the super high aspect ratios, $\Delta\xi / \Delta\eta$, of meshes for high Reynolds number flow, typical of aerodynamic problems, proper support will given to the viscous terms with derivatives with respect to η and not, in general to those with respect to ξ. One has the choice of deleting the viscous terms with derivatives with respect to ξ from the governing equations or to let the mesh do the pruning. Both approaches are given below. The author prefers to approximate all the terms of the Navier-

Stokes equations, knowing that some may not receive proper mesh support, for the same reason as the presence of a small hammer within a coffin may provide a feeling of added security.

17.5.1 Thin Layer Navier-Stokes Flux Vectors in General Curvilinear Coordinates

The Thin Layer Navier-Stokes (TLNS) equations for a flow past a solid surface aligned with the ξ coordinate direction, as shown for example in the Fig.17.2, for which the viscous derivatives with respect to η are much more important than those with respect to ξ,

$$\frac{\partial}{\partial \eta}_{viscous} \quad >> \quad \frac{\partial}{\partial \xi}_{viscous}$$

can be written as in Equation (17.3) with the term containing $M_{\xi\xi}$ removed and the corresponding explicit flux vectors given by

$$F'^{TLNS}_{i+1/2,j} = F'_{Euler_{i+1/2,j}}$$

$$\text{and} \qquad G'^{TLNS}_{i,j+1/2} = G'_{Euler_{i,j+1/2}} - M_{\eta\eta_{i,j+1/2}} \frac{D_+ \cdot}{\Delta \eta} V_{i,j}$$

where again the "dots" indicate that the difference operators apply to all factors to the right.

17.5.2 Full Navier-Stokes Flux Vectors in General Curvilinear Coordinates

The full Navier-Stokes flux vectors are given by

$$F'_{i+1/2,j} = F'_{Euler_{i+1/2,j}} - M_{\xi\xi_{i+1/2,j}} \frac{D_+ \cdot}{\Delta \xi} V_{i,j} - M_{\xi\eta_{i+1/2,j}} \frac{D_o \cdot}{\Delta \eta} \frac{1}{2}\left(V_{i,j} + V_{i+1,j}\right)$$

$$G'_{i,j+1/2} = G'_{Euler_{i,j+1/2}} - M_{\eta\xi_{i,j+1/2}} \frac{D_o \cdot}{\Delta \xi} \frac{1}{2}\left(V_{i,j} + V_{i,j+1}\right) - M_{\eta\eta_{i,j+1/2}} \frac{D_+ \cdot}{\Delta \eta} V_{i,j}$$

The difference operators $\dfrac{D_o \cdot}{\Delta \xi}$ and $\dfrac{D_o \cdot}{\Delta \eta}$ are central difference operators (see Sec.3.3) with respect to ξ and η, respectively. The viscous flux terms are each centered about their respective flux surfaces and are therefore second order accurate.

17.6 Implicit Algorithm for Full Navier-Stokes Equations

An implicit algorithm for solving the full Navier-Stokes equations for compressible viscous flow in arbitrary curvilinear coordinates, similar to that given earlier in Chapter16 for Cartesian coordinates, is

$$\left\{ I + \alpha \frac{\Delta t}{V_{i,j}} \left(\frac{D_- \cdot}{\Delta \xi} \overline{A'}^n_{+i+1/2,j} + \frac{D_+ \cdot}{\Delta \xi} \overline{A'}^n_{-i-1/2,j} + \frac{D_- \cdot}{\Delta \eta} \overline{B'}^n_{+i,j+1/2} + \frac{D_+ \cdot}{\Delta \eta} \overline{B'}^n_{-i,j-1/2} \right) \right.$$

$$\left. - \frac{\Delta t}{V_{i,j}} \left(\frac{D_- \cdot}{\Delta \xi} M_{\xi\xi_{i+1/2,j}} \frac{D_+ \cdot}{\Delta \xi} + \frac{D_- \cdot}{\Delta \eta} M_{\eta\eta_{i,j+1/2}} \frac{D_+ \cdot}{\Delta \eta} \right) N_{i,j} \right\} \delta U^{n+1}_{i,j} = \Delta U^{n+1}_{i,j}$$

$$= -\frac{\Delta t}{V_{i,j}} \left(\frac{F'^n_{i+1/2,j} - F'^n_{i-1/2,j}}{\Delta \xi} + \frac{G'^n_{i,j+1/2} - G'^n_{i,j-1/2}}{\Delta \eta} \right)_{Euler} \tag{17.4}$$

$$+ \frac{\Delta t}{V_{i,j}} \frac{D_- \cdot}{\Delta \xi} \left(M_{\xi\xi_{i+1/2,j}} \frac{D_+ \cdot}{\Delta \xi} V_{i,j} + M_{\xi\eta_{i+1/2,j}} \frac{D_o \cdot 1}{\Delta \eta} \frac{1}{2} \left(V_{i,j} + V_{i+1,j} \right) \right)$$

$$+ \frac{\Delta t}{V_{i,j}} \frac{D_- \cdot}{\Delta \eta} \left(M_{\eta\xi_{i,j+1/2}} \frac{D_o \cdot 1}{\Delta \xi} \frac{1}{2} \left(V_{i,j} + V_{i,j+1} \right) + M_{\eta\eta_{i,j+1/2}} \frac{D_+ \cdot}{\Delta \eta} V_{i,j} \right)$$

again where $\alpha = 1$ is used for first order flux approximations and $\alpha \geq 3/2$ is recommended for higher order flux approximations on the right hand side of the equation. The spatial inviscid terms on the implicit side of the equation are only first order accurate and need use only data from grid points above, below, left and right of the central grid point at (i,j). Also, the procedure is of first order accuracy in time. This is an efficient procedure for obtaining steady state solutions to higher accuracy than first if the right hand side of the equation uses higher than first order accurate approximations. Fully second order accurate or higher procedures for unsteady flows will be presented later. Note that the cross derivative viscous terms have been left out of the above equation on the left hand side, although the full set of Navier-Stokes terms are included on the right hand side. Only the pure ξ and η derivatives appear on the implicit side. Again, as in Chapter 16, this is all that is required for stability for unlimited time step size and that to include the mixed derivative viscous terms would unnecessarily require an increase of the number of implicit points of the mesh star from the present number of five. The present implicit algorithm is suitable for solving the complete Navier-Stokes equations in an arbitrary coordinate system.

The algorithm can be expressed as a block pentadiagonal matrix equation

$$\overline{B}_{i,j} \delta U^{n+1}_{i,j+1} + \overline{A}_{i,j} \delta U^{n+1}_{i,j} + \overline{C}_{i,j} \delta U^{n+1}_{i,j-1} + \overline{D}_{i,j} \delta U^{n+1}_{i+1,j} + \overline{E}_{i,j} \delta U^{n+1}_{i-1,j} = \Delta U^n_{i,j} \tag{17.5}$$

The block element matrices $\overline{A}_{i,j}$, $\overline{B}_{i,j}$, $\overline{C}_{i,j}$, $\overline{D}_{i,j}$ and $\overline{E}_{i,j}$ are

$$\overline{A}_{i,j} = I + \frac{\Delta t}{V_{i,j}\Delta\xi}\left(\alpha\overline{A}'^{n}_{+i+1/2,j} - \alpha\overline{A}'^{n}_{-i-1/2,j} + \frac{1}{\Delta\xi}\left(M_{\xi\xi_{i+1/2,j}} + M_{\xi\xi_{i-1/2,j}}\right)N^{n}_{i,j}\right)$$

$$+ \frac{\Delta t}{V_{i,j}\Delta\eta}\left(\alpha\overline{B}'^{n}_{+i,j+1/2} - \alpha\overline{B}'^{n}_{-i,j-1/2} + \frac{1}{\Delta\eta}\left(M_{\eta\eta_{i,j+1/2}} + M_{\eta\eta_{i,j-1/2}}\right)N^{n}_{i,j}\right), \qquad (17.6)$$

$$\overline{B}_{i,j} = \frac{\Delta t}{V_{i,j}\Delta\eta}\left(\alpha\overline{B}'^{n}_{-i,j+1/2} - \frac{1}{\Delta\eta}M_{\eta\eta_{i,j+1/2}}N^{n}_{i,j+1}\right), \qquad \overline{C}_{i,j} = \frac{\Delta t}{V_{i,j}\Delta\eta}\left(-\alpha\overline{B}'^{n}_{+i,j-1/2} - \frac{1}{\Delta\eta}M_{\eta\eta_{i,j-1/2}}N^{n}_{i,j-1}\right),$$

$$\overline{D}_{i,j} = \frac{\Delta t}{V_{i,j}\Delta\xi}\left(\alpha\overline{A}'^{n}_{-i+1/2,j} - \frac{1}{\Delta\xi}M_{\xi\xi_{i+1/2,j}}N^{n}_{i+1,j}\right) \quad and \quad \overline{E}_{i,j} = \frac{\Delta t}{V_{i,j}\Delta\xi}\left(-\alpha\overline{A}'^{n}_{+i-1/2,j} - \frac{1}{\Delta\xi}M_{\xi\xi_{i-1/2,j}}N^{n}_{i-1,j}\right)$$

17.7 Evaluation of Metric and Flow Derivative Terms

The evaluation of the metric terms and the viscous flow derivative terms on a computational mesh will now be discussed from the perspective of both the finite difference and finite volume points of view.

17.7.1 Finite Difference Approach

Consider a section of a finite difference mesh as shown above. The finite difference approach defines both the flow variables and (x, y) coordinate values at the same set of (ξ,η) mesh points. The flow variables and metric values are thus co-located. A volume about mesh point (i, j) is shown in the adjacent figure by the dashed lines with surfaces at $\xi = i \pm 1/2$ and $\eta = j \pm 1/2$. These are the surfaces at which the rotated flux terms F' and G' need to be evaluated.
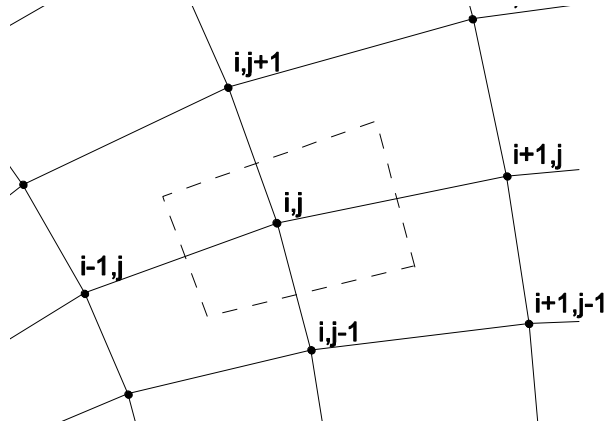
Figure 17.4 Finite difference mesh

The metric volume term $V_{i,j}$ is evaluated by

$$V_{i,j} = \left(\frac{\partial x}{\partial\xi}\frac{\partial y}{\partial\eta} - \frac{\partial x}{\partial\eta}\frac{\partial y}{\partial\xi}\right)_{i,j} = \frac{\left(x_{i+1,j} - x_{i-1,j}\right)}{2\Delta\xi}\frac{\left(y_{i,j+1} - y_{i,j-1}\right)}{2\Delta\eta} - \frac{\left(x_{i,j+1} - x_{i,j-1}\right)}{2\Delta\eta}\frac{\left(y_{i+1,j} - y_{i-1,j}\right)}{2\Delta\xi}$$

At the flux surfaces $\xi = i+1/2$ and $\eta = j+1/2$ derivatives of x and y with respect to ξ and η need to be determined for the metric terms. Also, derivatives of u, v and T need to be determined for the viscous terms. The flow variable v will be used to represent derivatives of all the flow variables.

At flux surface $\xi = i+1/2$

$$\left.\frac{\partial x}{\partial \xi}\right|_{i+1/2} = \frac{x_{i+1,j} - x_{i,j}}{\Delta \xi}, \qquad \left.\frac{\partial x}{\partial \eta}\right|_{i+1/2} = \frac{1}{2}\left(\frac{x_{i,j+1} - x_{i,j-1}}{2\Delta \eta} + \frac{x_{i+1,j+1} - x_{i+1,j-1}}{2\Delta \eta}\right),$$

$$\left.\frac{\partial y}{\partial \xi}\right|_{i+1/2} = \frac{y_{i+1,j} - y_{i,j}}{\Delta \xi}, \qquad \left.\frac{\partial y}{\partial \eta}\right|_{i+1/2} = \frac{1}{2}\left(\frac{y_{i,j+1} - y_{i,j-1}}{2\Delta \eta} + \frac{y_{i+1,j+1} - y_{i+1,j-1}}{2\Delta \eta}\right),$$

$$\left.\frac{\partial v}{\partial \xi}\right|_{i+1/2} = \frac{v_{i+1,j} - v_{i,j}}{\Delta \xi} \qquad \text{and} \qquad \left.\frac{\partial v}{\partial \eta}\right|_{i+1/2} = \frac{1}{2}\left(\frac{v_{i,j+1} - v_{i,j-1}}{2\Delta \eta} + \frac{v_{i+1,j+1} - v_{i+1,j-1}}{2\Delta \eta}\right),$$

At flux surface $\eta = j+1/2$

$$\left.\frac{\partial x}{\partial \xi}\right|_{j+1/2} = \frac{1}{2}\left(\frac{x_{i+1,j} - x_{i-1,j}}{2\Delta \xi} + \frac{x_{i+1,j+1} - x_{i-1,j+1}}{2\Delta \xi}\right), \qquad \left.\frac{\partial x}{\partial \eta}\right|_{j+1/2} = \frac{x_{i,j+1} - x_{i,j}}{\Delta \eta},$$

$$\left.\frac{\partial y}{\partial \xi}\right|_{j+1/2} = \frac{1}{2}\left(\frac{y_{i+1,j} - y_{i-1,j}}{2\Delta \xi} + \frac{y_{i+1,j+1} - y_{i-1,j+1}}{2\Delta \xi}\right), \qquad \left.\frac{\partial y}{\partial \eta}\right|_{j+1/2} = \frac{y_{i,j+1} - y_{i,j}}{\Delta \eta},$$

$$\left.\frac{\partial v}{\partial \xi}\right|_{j+1/2} = \frac{1}{2}\left(\frac{v_{i+1,j} - v_{i-1,j}}{2\Delta \xi} + \frac{v_{i+1,j+1} - v_{i-1,j+1}}{2\Delta \xi}\right), \qquad \text{and} \qquad \left.\frac{\partial v}{\partial \eta}\right|_{j+1/2} = \frac{v_{i,j+1} - v_{i,j}}{\Delta \eta},$$

17.7.2 Finite Volume Approach

Consider a section of a finite volume mesh as shown above. The finite volume approach defines the flow variables at the centroids of the finite volumes formed by the mesh lines and (x, y) coordinate locations at the intersections of the grid lines. The flow variables and metric values are not physically co-located as in the finite difference approach.

10
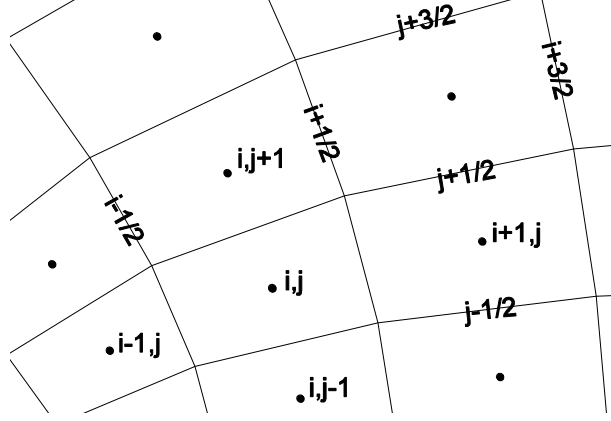
Figure 17.5 Finite volume mesh

The metric volume term $V_{i,j}$ is evaluated by

$$V_{i,j} = \frac{1}{2}\left(\frac{\partial x}{\partial \xi}\bigg|_{j-1/2} \frac{\partial y}{\partial \eta}\bigg|_{i+1/2} - \frac{\partial x}{\partial \eta}\bigg|_{i+1/2} \frac{\partial y}{\partial \xi}\bigg|_{j-1/2} \right) + \frac{1}{2}\left(\frac{\partial x}{\partial \xi}\bigg|_{j+1/2} \frac{\partial y}{\partial \eta}\bigg|_{i-1/2} - \frac{\partial x}{\partial \eta}\bigg|_{i-1/2} \frac{\partial y}{\partial \xi}\bigg|_{j+1/2} \right)$$

$$= \frac{1}{2}\frac{\left(x_{i+1/2,j-1/2} - x_{i-1/2,j-1/2} \right)}{\Delta\xi} \frac{\left(y_{i+1/2,j+1/2} - y_{i+1/2,j-1/2} \right)}{\Delta\eta} - \frac{1}{2}\frac{\left(x_{i+1/2,j+1/2} - x_{i+1/2,j-1/2} \right)}{\Delta\eta} \frac{\left(y_{i+1/2,j-1/2} - y_{i-1/2,j-1/2} \right)}{\Delta\xi}$$

$$+ \frac{1}{2}\frac{\left(x_{i+1/2,j+1/2} - x_{i-1/2,j+1/2} \right)}{\Delta\xi} \frac{\left(y_{i-1/2,j+1/2} - y_{i-1/2,j-1/2} \right)}{\Delta\eta} - \frac{1}{2}\frac{\left(x_{i-1/2,j+1/2} - x_{i-1/2,j-1/2} \right)}{\Delta\eta} \frac{\left(y_{i+1/2,j+1/2} - y_{i-1/2,j+1/2} \right)}{\Delta\xi}$$

The above expression is equivalent to that given in Sec.7.4, where the half integer subscripts above were replaced by their computer program array storage indices, i.e., $i \leftarrow i-1/2$ and $j \leftarrow j-1/2$ etc.

The derivatives at the flux surfaces $\xi = i+1/2$ and $\eta = j+1/2$ of x, y and flow variable v with respect to ξ and η are given below for the finite volume approach.

At flux surface $\xi = i+1/2$

$$\frac{\partial x}{\partial \xi}\bigg|_{i+1/2} = \frac{1}{2}\left(\frac{x_{i+3/2,j-1/2} - x_{i-1/2,j-1/2}}{2\Delta\xi} + \frac{x_{i+3/2,j+1/2} - x_{i-1/2,j+1/2}}{2\Delta\xi} \right), \qquad \frac{\partial x}{\partial \eta}\bigg|_{i+1/2} = \frac{x_{i+1/2,j+1/2} - x_{i+1/2,j-1/2}}{\Delta\eta},$$

$$\frac{\partial y}{\partial \xi}\bigg|_{i+1/2} = \frac{1}{2}\left(\frac{y_{i+3/2,j-1/2} - y_{i-1/2,j-1/2}}{2\Delta\xi} + \frac{y_{i+3/2,j+1/2} - y_{i-1/2,j+1/2}}{2\Delta\xi} \right), \qquad \frac{\partial y}{\partial \eta}\bigg|_{i+1/2} = \frac{y_{i+1/2,j+1/2} - y_{i+1/2,j-1/2}}{\Delta\eta},$$

$$\frac{\partial v}{\partial \xi}\bigg|_{i+1/2} = \frac{v_{i+1,j} - v_{i,j}}{\Delta\xi} \qquad\qquad \text{and} \qquad\qquad \frac{\partial v}{\partial \eta}\bigg|_{i+1/2} = \frac{1}{2}\left(\frac{v_{i,j+1} - v_{i,j-1}}{2\Delta\eta} + \frac{v_{i+1,j+1} - v_{i+1,j-1}}{2\Delta\eta} \right),$$

$$\left.\frac{\partial x}{\partial \xi}\right|_{j+1/2} = \frac{x_{i+1/2,j+1/2} - x_{i-1/2,j+1/2}}{\Delta \xi}, \qquad \left.\frac{\partial x}{\partial \eta}\right|_{j+1/2} = \frac{1}{2}\left(\frac{x_{i-1/2,j+3/2} - x_{i-1/2,j-1/2}}{2\Delta \eta} + \frac{x_{i+1/2,j+3/2} - x_{i+1/2,j-1/2}}{2\Delta \eta}\right),$$

$$\left.\frac{\partial y}{\partial \xi}\right|_{j+1/2} = \frac{y_{i+1/2,j+1/2} - y_{i-1/2,j+1/2}}{\Delta \xi}, \qquad \left.\frac{\partial y}{\partial \eta}\right|_{j+1/2} = \frac{1}{2}\left(\frac{y_{i-1/2,j+3/2} - y_{i-1/2,j-1/2}}{2\Delta \eta} + \frac{y_{i+1/2,j+3/2} - y_{i+1/2,j-1/2}}{2\Delta \eta}\right),$$

$$\left.\frac{\partial v}{\partial \xi}\right|_{j+1/2} = \frac{1}{2}\left(\frac{v_{i+1,j} - v_{i-1,j}}{2\Delta \xi} + \frac{v_{i+1,j+1} - v_{i-1,j+1}}{2\Delta \xi}\right), \qquad \text{and} \qquad \left.\frac{\partial v}{\partial \eta}\right|_{j+1/2} = \frac{v_{i,j+1} - v_{i,j}}{\Delta \eta},$$

17.8 Implicit Boundary Conditions at Solid Walls

Boundary conditions at solid walls for the Navier-Stokes equations are given in Sec.12.5. This section will present techniques for their implementation in an implicit algorithm. For convenience we will consider a body fitted mesh with the body surface aligned with a ξ coordinate line, i.e., a line of constant η, with $\eta = 1$ for finite difference and $\eta = 1 + 1/2$ for the finite volume approach.
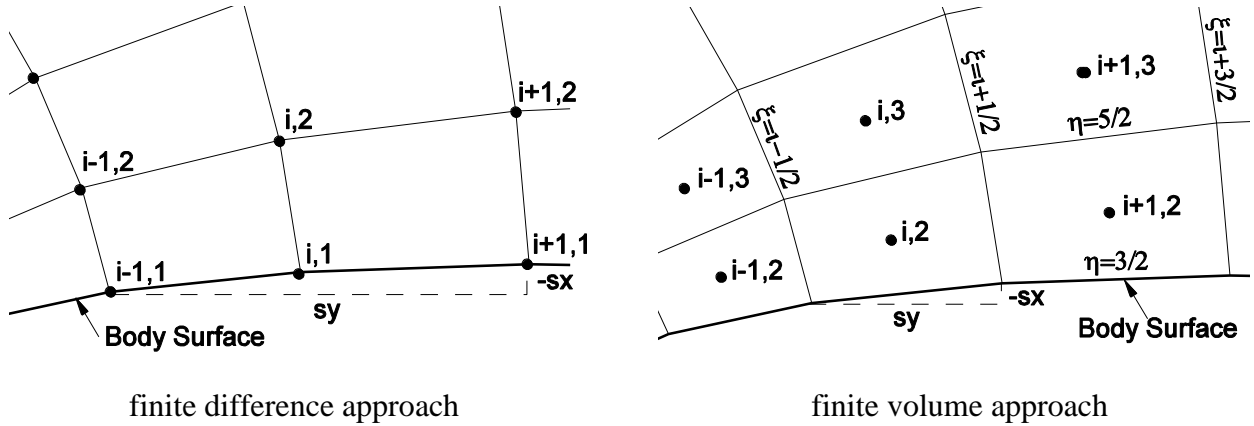
finite difference approach   finite volume approach
Figure 17.6 Boundary condition implementation for finite difference and finite volume approaches

17.8.1 Euler flux boundary condition

Again, "all you need is p" for the inviscid Euler equations. For the Navier-Stokes equations at a *wall* point "i" $p_{i,1} = p_{i,2}$.

Therefore
$$G'^{n}_{Euler_{Wall}} = \begin{bmatrix} 0 \\ \left.sx\right|_{wall} p_{i,2}^{n} \\ \left.sy\right|_{wall} p_{i,2}^{n} \\ 0 \end{bmatrix}$$

$$\underline{\text{finite difference approach}} \qquad\qquad \underline{\text{finite volume approach}}$$

where $sx|_{wall} = -\Delta\xi \left.\dfrac{\partial y}{\partial \xi}\right|_{wall} = -\dfrac{1}{2}\left(y_{i+1,1} - y_{i-1,1}\right)$ or $sx|_{wall} = -\Delta\xi \left.\dfrac{\partial y}{\partial \xi}\right|_{wall} = -\left(y_{i+1/2,3/2} - y_{i-1/2,3/2}\right),$

and $sy|_{wall} = +\Delta\xi \left.\dfrac{\partial x}{\partial \xi}\right|_{wall} = +\dfrac{1}{2}\left(x_{i+1,1} - x_{i-1,1}\right)$ or $sy|_{wall} = +\Delta\xi \left.\dfrac{\partial x}{\partial \xi}\right|_{wall} = +\left(x_{i+1/2,3/2} - x_{i-1/2,3/2}\right).$

This boundary condition is implemented in the implicit algorithm for the Navier-Stokes equations by replacing the Euler part of the flux term $G'^{n}_{i,j-1/2}$ for $j = 2$ on the right hand side of Equation (17.4) as follows.

$$G'^{n}_{Euler_{i,3/2}} \leftarrow G'^{n}_{Euler_{wall}}$$

Similarly, changes must also be made to the left hand side of Equation (17.4). In "delta law" form the corresponding implicit term is given by

$$G'^{n+1}_{Euler_{wall}} = G'^{n}_{Euler_{wall}} + \delta G'_{Euler_{wall}}$$

$$\delta G'_{Euler_{Wall}} = \begin{bmatrix} 0 \\ sx|_{wall}\,\delta p_{i,2} \\ sy|_{wall}\,\delta p_{i,2} \\ 0 \end{bmatrix} = \frac{\partial G'_{Euler_{Wall}}}{\partial U}\delta U_{i,2} = B''_{i,3/2}\delta U_{i,2}$$

with

$$B''_{i,3/2} = (\gamma - 1)\begin{bmatrix} 0 & 0 & 0 & 0 \\ sx\dfrac{u^2 + v^2}{2} & -sxu & -sxv & sx \\ sy\dfrac{u^2 + v^2}{2} & -syu & -syv & sy \\ 0 & 0 & 0 & 0 \end{bmatrix}^n_{i,2}$$

The block element matrices defined by Equation (17.5) need to modified as follows at $j = 2$, the interior point adjacent to the wall.

1) In element $\overline{A}_{i,2}$ replace $\overline{B}'^{n}_{-_{i,3/2}}$ with $B''_{i,3/2}$ given above.

2) In element $\overline{C}_{i,2}$ remove $\overline{B}'^{n}_{+_{i,3/2}}$.

17.8.2 Viscous flux boundary condition
See Sec.12.5.3, Sec.16.3.2 and Sec.16.5 for boundary conditions for the viscous terms for Cartesian meshes. The viscous boundary conditions for an arbitrary curvilinear coordinate system are similar,

but the velocity fields may need to be rotated for velocity "slip" boundaries. Along solid walls the "no slip" boundary condition implies that the velocity components are zero along the boundary. But, as examples, for boundaries that are 1) ahead of the leading edge of a flat plate and lying in the plane of the plate or 2) a symmetry line or a streamline of the flow, the tangential velocity component to the boundary is not subject to the "no slip" rule. General boundary conditions for viscous flow, including both "slip" and "no slip" are presented in Sec.17.9.2. For the present, we assume that the boundary is a "no slip" flat or curvilinear wall with either adiabatic or isothermal temperature boundary conditions.

For the finite difference approach, we obtain

$$V_{i,1} = \begin{bmatrix} \rho \\ u \\ v \\ T \end{bmatrix}_{i,1} = \begin{bmatrix} \rho \\ 0 \\ 0 \\ tT_{i,2} + (1-t)T_{wall} \end{bmatrix}$$

where $t=1$ for adiabatic walls and $t=0$ for isothermal walls at temperature T_{wall}.

For the finite volume approach

$$V_{i,1} = \begin{bmatrix} \rho \\ u \\ v \\ T \end{bmatrix}_{i,1} = \begin{bmatrix} \rho \\ -u_{i,2} \\ -v_{i,2} \\ tT_{i,2} + (1-t)T_{wall} \end{bmatrix}$$

where again $t=1$ for adiabatic walls but -1 for isothermal walls. The variable ρ appears in the above vectors for V for convenience but will not be used by the viscous term boundary condition because of the row of "zeros" appearing in the top line of the viscous coefficient matrices M_{xx} etc.. No boundary condition is required for ρ either for the Euler terms at solid walls.

Both cases can be put into the following "delta law" form for use on the left hand side of the implicit matrix equation.

$$\delta V_{i,1} = \begin{bmatrix} \delta\rho \\ \delta u \\ \delta v \\ \delta T \end{bmatrix}_{i,1} = \begin{bmatrix} 1 & 0 & 0 & 0 \\ 0 & -e & 0 & 0 \\ 0 & 0 & -e & 0 \\ 0 & 0 & 0 & t \end{bmatrix} \delta V_{i,2} = E \begin{bmatrix} \delta\rho \\ \delta u \\ \delta v \\ \delta T \end{bmatrix}_{i,2}$$

where t is defined as before and $e=0$ for the finite difference approach or $e=1$ for the finite volume approach.

14

Combining the Euler implicit boundary condition modification of the last subsection and the present viscous implicit boundary condition yields the following modification to the block element matrices $\overline{A}_{i,j}$ and $\overline{C}_{i,j}$ defined by Equation (17.5) at $j=2$.

$$\overline{A}_{i,2} = I + \frac{\Delta t}{V_{i,j}\Delta\xi}\left(\alpha\overline{A'}^{n}_{+i+1/2,2} - \alpha\overline{A'}^{n}_{-i-1/2,2} + \frac{1}{\Delta\xi}\left(M_{\xi\xi_{i+1/2,2}} + M_{\xi\xi_{i-1/2,2}}\right)N^{n}_{i,2}\right)$$
$$+ \frac{\Delta t}{V_{i,j}\Delta\eta}\left(\alpha\overline{B'}^{n}_{+i,2+1/2} - \alpha B''^{n}_{-i,3/2} + \frac{1}{\Delta\eta}\left(M_{\eta\eta_{i,2+1/2}} + M_{\eta\eta_{i,2-1/2}}\left(I - E\right)\right)N^{n}_{i,j}\right),$$

and $\qquad \overline{C}_{i,2} = 0$

The matrix Equation (17.4) then becomes for $j=2$

$$\overline{B}_{i,2}\delta U^{n+1}_{i,3} + \overline{A}_{i,2}\delta U^{n+1}_{i,2} + \overline{D}_{i,2}\delta U^{n+1}_{i+1,2} + \overline{E}_{i,2}\delta U^{n+1}_{i-1,2} = \Delta U^{n}_{i,2}$$

Note that all dependence upon the boundary value $\delta U^{n+1}_{i,1}$ has been removed. The implicit boundary conditions have been fully embedded within the matrix equation. Similar procedures can be used for other implicit boundary conditions along other computational coordinate surfaces.

17.8.3 The Navier-Stokes Equations in Axi-Symmetric Arbitrary Coordinates

See Sec.14.5 for the surface area and volume changes required to extend a two dimensional plane symmetric algorithm for solving the Euler equations into an axisymmetric one. The additional surface stress term also given there for the Euler equations now needs to be rewritten to include the viscous stress also acting on the volume faces orthogonal to the θ-direction. The Euler equations written for a cylindrical coordinate system in the $x-y$ plane, where y is the radial coordinate, were given at the end of Sec.14.52. The Navier-Stokes equations, written in a cylindrical coordinate system becomes

$$\frac{\partial U}{\partial t} + \frac{\partial(F_{Euler} + F_{viscous})}{\partial x} + \frac{1}{y}\frac{\partial y(G_{Euler} + G_{viscous})}{\partial y} = Q^{axi} = \frac{1}{y}\begin{bmatrix} 0 \\ 0 \\ p - \sigma_{\theta\theta} \\ 0 \end{bmatrix}$$

The stress tensor for the viscous terms is given by $\tau_{ij} = \mu\left(\frac{\partial u_i}{\partial x_j} + \frac{\partial u_j}{\partial x_i}\right) + \delta_{ij}\lambda\vec{\nabla}\cdot\vec{q}$, where $\vec{q}$ is the velocity vector. For 2-D plane symmetric flow $\vec{\nabla}\cdot\vec{q} = \frac{\partial u_k}{\partial x_k} = \frac{\partial u}{\partial x} + \frac{\partial v}{\partial y}$ For axisymmetric flow $\vec{\nabla}\cdot\vec{q} = \frac{\partial u}{\partial x} + \frac{\partial v}{\partial y} + \frac{v}{y}$. The term $\sigma_{\theta\theta} = 2\mu\frac{v}{y} + \lambda\vec{\nabla}\cdot\vec{q}$. Therefore, the equation for axisymmetric flow in arbitrary, but axisymmetric, coordinates, using the quantities defined in Sec.14.5 plus redefining of the divergence of velocity as above, becomes

$$\frac{\partial U}{\partial t} + \frac{1}{V^{axi}}\frac{\partial F'^{axi}}{\partial \xi} + \frac{1}{V^{axi}}\frac{\partial G'^{axi}}{\partial \eta} = Q^{axi} = \frac{\Delta S^{axi}}{V^{axi}}\begin{bmatrix} 0 \\ 0 \\ p - \sigma_{\theta\theta} \\ 0 \end{bmatrix}$$

The Jacobian of Q^{axi} with respect to U needed for implicit methods becomes

$$\frac{\partial Q^{axi}}{\partial U} = \frac{\Delta S^{axi}}{V^{axi}}\left\{\begin{bmatrix} 0 & 0 & 0 & 0 \\ 0 & 0 & 0 & 0 \\ \alpha\beta & -u\beta & -v\beta & \beta \\ 0 & 0 & 0 & 0 \end{bmatrix} - \frac{\lambda + 2\mu}{\overline{y}\rho}\begin{bmatrix} 0 & 0 & 0 & 0 \\ 0 & 0 & 0 & 0 \\ -v & 0 & 1 & 0 \\ 0 & 0 & 0 & 0 \end{bmatrix}\right\},$$

where $\alpha = \dfrac{u^2 + v^2}{2}$ and $\beta = \gamma - 1$. The equation for $\overline{A}_{i,j}$, Eq.17.6, needs an additional term for axisymmetric flow, i.e. $\overline{A}_{i,j}^{axi} = \overline{A}_{i,j} - \Delta t\dfrac{\partial Q^{axi}}{\partial U}$. The viscous part of the Jacobian above included the term $-(\lambda + 2\mu)\dfrac{v}{y}$ of $\sigma_{\theta\theta}$, but the derivative terms were neglected. If they were included, changes would need to be made to the other matrices defined by Eq.17.6.

17.9 Application: Viscous Flow Past a Compression Corner
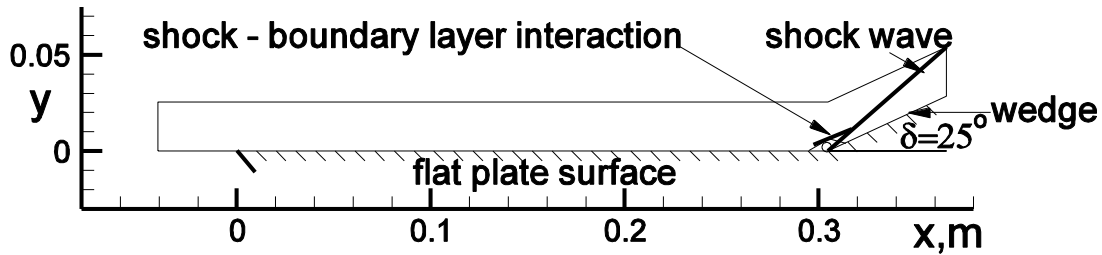
Figure 17.7 Flow field past a compression corner

Figure 17.7 shows the flow field setup for flow about a wedge sitting upon a flat plate. This flow was solved by Joe Shang and W.L. Hankey Jr. (AIAA Journal, Vol.13, No.10, October 1975, pp. 1368-1374), using a relaxation of the Cebeci-Smith turbulence model (see Sec.15.6). Figure 17.8 shows the flow field setup for inviscid flow about the wedge. Details for viscous flow about the wedge are sketched in Figure 17.9, showing the interaction of the shock wave with the boundary layer. The fluid adjacent to the wall, having insufficient momentum to negotiate the adverse pressure gradient, separates from the wall and then reattaches downstream of the corner, trapping a slow recirculating region of fluid.
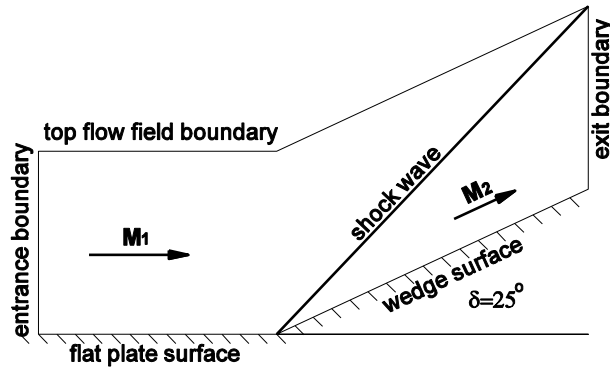
Figure 17.8 Inviscid flow past a wedge
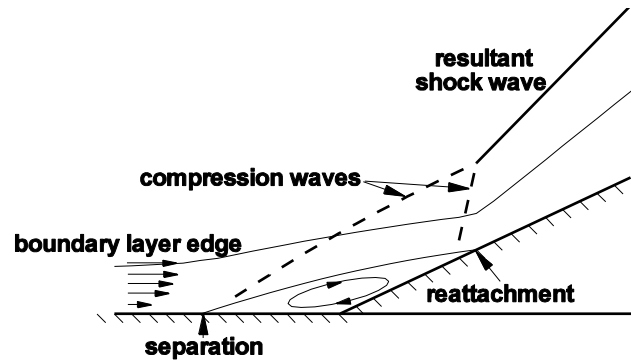
Figure 17.9 Sketch of viscous flow past a wedge

17.9.1 Exercise: Flow Past a Compression Corner

Solve the two dimensional Navier-Stokes equations for turbulent supersonic flow past a compression corner. The wedge angle is $\delta = 25^o$ and the free stream Mach number is $M_\infty = 2.96$. The length of the flat plate up to corner is $L = 1\,ft$ ($0.3048m$) and the Reynolds number $\text{Re}_L = 10^7$. Use either the Modified Steger-Warming or the Roe method for the Euler terms and central differencing of the viscous terms. Solve for both laminar and turbulent flow using the Baldwin-Lomax turbulence model (see Sec.15.7). Solve the resulting equations implicitly.

Approach

A two step approach will be used to calculate the flow past the compression corner. First, the flow past the flat plate is solved. Then, just ahead of the location for the corner, at about $x_0 = 0.9\,ft$, the flow conditions from the flat plate solution are used as the initial conditions for flow past the wedge.

17.9.2 Flat Plate Solution
17.9.2.1 Mesh for the Flat Plate

A 36x32 mesh is shown in Figure 17.10. This mesh consists of a fine stretched mesh, containing 20 mesh cells across or 21 points, joined smoothly to an equally spaced outer course mesh, containing 10 more cells to reach the top boundary of the flow field. The mesh is equally spaced in the x direction, with 30 mesh cells along the plate and 6 ahead of it, $\Delta x = L/30$.
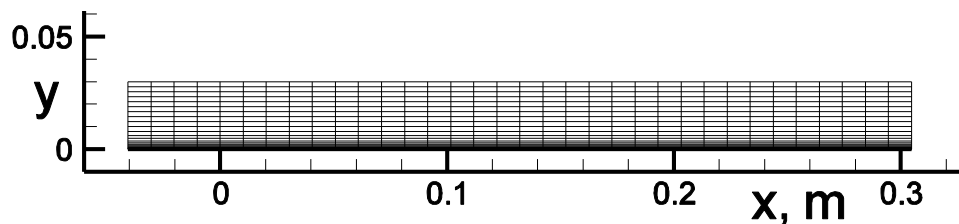
Figure 17.10 Mesh for flow past a flat plate

This mesh is similar to that discussed in Sec.16.9.2, using the compound stretching function. In this case $JL = 32$, $JLFM = 22$ and $H = 0.03m$. The boundary layer thickness and Δy_{min} are estimated below (see also Sec.16.9.1)

$$\delta(L) = \begin{cases} \dfrac{5L}{\sqrt{Re_L}}, & \text{laminar flow} \\[3mm] \dfrac{0.37L}{\left(Re_L\right)^{0.2}}, & \text{turbulent flow} \end{cases} \qquad \text{and} \qquad \Delta y_{\min} = \begin{cases} \delta(L)/30, & \text{laminar flow} \\[3mm] \delta(L)/300, & \text{turbulent flow} \end{cases}$$

The compound stretching function procedure calculates both the stretching exponent κ and the height of the fine mesh y_{fm}. A detail of the mesh near the leading edge of the flat plate is shown below.
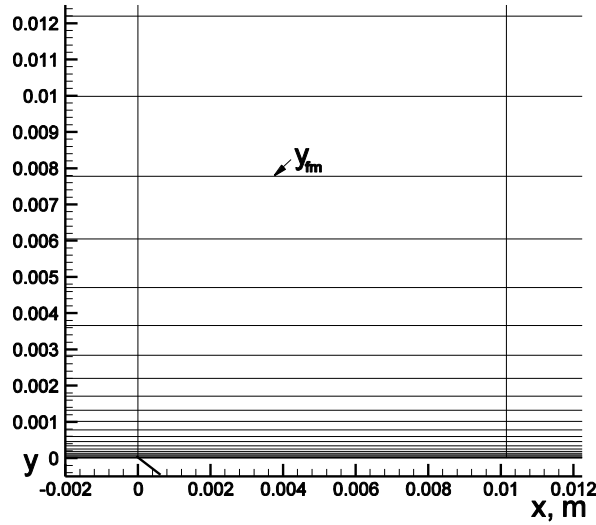
Figure 17.11 Mesh detail

17.9.2.2 Initial Conditions

Assume that the free stream temperature $T_\infty = 300^o K$. Then find the sound speed c_∞ and velocity $u_\infty = c_\infty M_\infty$. Use Sutherland's formula to obtain μ_∞ and the Reynolds number to find density ρ_∞. Start the calculation using uniform free stream flow.

17.9.2.3 Boundary Conditions

The conditions at the entrance and top boundaries are fixed at the uniform free stream values. The top boundary is assumed to be located far enough from the plate so that flow disturbances reaching and reflecting off of it are not expected to be significant. The implicit values for δU vanish along these two boundaries.

Along the lower boundary, solid wall boundary conditions are used downstream of the leading edge of the plate and *slip* conditions are used ahead. Boundary conditions along a solid wall are discussed in Sec.17.8 for both the Euler and viscous terms. The boundary conditions on the Euler part of the flux are the same for a *slip* or *no slip* boundary, but the viscous boundary conditions will be different. Only the normal component of velocity vanishes along a *slip* boundary and not all velocity components as for *no slip* walls. In our 2-D flow, let the components u'' and v'' be the

components tangential and normal to the lower boundary, respectively. Using the angle β defined in Sec.17.3,

$$u'' = \cos\beta\, u - \sin\beta\, v \quad and \quad v'' = \sin\beta\, u + \cos\beta\, v$$

The slip boundary condition for the viscous terms becomes $v''_{wall} = 0$ and $u''_{wall} = u''_{int.pt.}$, where u'' at the wall is set equal to the value at the nearest interior mesh point. We can combine the *slip* and *no slip* boundary conditions as follows, using the rotation matrix $R_{B'}$ defined in Sec.17.3.

$$V_{i,1} = R_{B'}^{-1}\begin{bmatrix}\rho\\ u''\\ v''\\ T\end{bmatrix}_{i,1} = R_{B'}^{-1}\underbrace{\begin{bmatrix}1 & 0 & 0 & 0\\ 0 & e_1 & 0 & 0\\ 0 & 0 & e_2 & 0\\ 0 & 0 & 0 & t\end{bmatrix}}_{E} R_{B'}\begin{bmatrix}\rho\\ u\\ v\\ T\end{bmatrix}_{i,2} + \begin{bmatrix}0\\ 0\\ 0\\ (1-t)T_{wall}\end{bmatrix} \quad and \quad \delta V_{i,1} = R_{B'}^{-1}E\,R_{B'}\delta V_{i,2}$$

where

(a) <u>for the finite difference approach</u>

$$e_1 = \begin{cases}1, & for\ slip\ boundaries\\ 0, & for\ no\ slip\ boundaries\end{cases}$$

$$e_2 = \begin{cases}0, & for\ slip\ boundaries\\ 0, & for\ no\ slip\ boundaries\end{cases}$$

$$t = \begin{cases}1, & for\ adiabatic\ or\ slip\ boundaries\\ 0, & for\ isothermal\ no\ slip\ boundaries\end{cases}$$

(b) <u>for the finite volume approach</u>

$$e_1 = \begin{cases}1, & for\ slip\ boundaries\\ -1, & for\ no\ slip\ boundaries\end{cases}$$

$$e_2 = \begin{cases}-1, & for\ slip\ boundaries\\ -1, & for\ no\ slip\ boundaries\end{cases}$$

$$t = \begin{cases}1, & for\ adiabatic\ or\ slip\ boundaries\\ -1, & for\ isothermal\ no\ slip\ boundaries\end{cases}$$

The implicit embedded boundary condition for this general viscous case, including both "slip" and "no slip" cases requires a change from that given in Sec.17.8.2, as follows.

$$\overline{A}_{i,2} = I + \frac{\Delta t}{V_{i,j}\Delta\xi}\left(\alpha\overline{A}'^{n}_{+i+1/2,2} - \alpha\overline{A}'^{n}_{-i-1/2,2} + \frac{1}{\Delta\xi}\left(M_{\xi\xi_{i+1/2,2}} + M_{\xi\xi_{i-1/2,2}}\right)N^{n}_{i,2}\right)$$

$$+ \frac{\Delta t}{V_{i,j}\Delta\eta}\left(\alpha\overline{B}'^{n}_{+i,2+1/2} - \alpha B''^{n}_{-i,3/2} + \frac{1}{\Delta\eta}\left(M_{\eta\eta_{i,2+1/2}} + M_{\eta\eta_{i,2-1/2}}\left(I - R_{B'}^{-1}E\,R_{B'}\right)\right)N^{n}_{i,j}\right)$$

Supersonic boundary conditions are used along the exit plane. Exit boundary conditions are discussed in Sec.12.4. For the present case the flow will exit supersonically and the boundary layer will be attached. Therefore, it will be very difficult for boundary condition error to propagate upstream and a simple shift condition, $U^{n}_{I,j} = U^{n}_{I-1,j}$ and $\delta U^{n}_{I,j} = \delta U^{n}_{I-1,j}$, at the exit should suffice.

17.9.2.4 Time Step Size:
The time step for an explicit method solving the Navier-Stokes equations in two dimensional arbitrary curvilinear coordinates is

$$\Delta t_{exp} \leq \min_{i,j} \left\{ \frac{V}{\left| \vec{q} \cdot \vec{s}_\xi \right| + \left| \vec{q} \cdot \vec{s}_\eta \right| + c\sqrt{\left| s_\xi \right|^2 + \left| s_\eta \right|^2} + \frac{4\mu}{\rho V}\left(\left| s_\xi \right|^2 + 2\left| s_\xi \right| \left| s_\eta \right| + \left| s_\eta \right|^2 \right)} \right\}_{i,j}$$

where $\quad \vec{q} = u\,\vec{i}_x + v\,\vec{i}_y, \quad \vec{s}_\xi = \frac{\partial y}{\partial \eta}\Delta\eta\,\vec{i}_x - \frac{\partial x}{\partial \eta}\Delta\eta\,\vec{i}_y \quad and \quad \vec{s}_\eta = -\frac{\partial y}{\partial \xi}\Delta\xi\,\vec{i}_x + \frac{\partial x}{\partial \xi}\Delta\xi\,\vec{i}_y$

As in Sec.16.5 for the problem of laminar flow past a flat plate, if all the terms are treated implicitly the time step is only expected to be limited by the non-linearity of the Navier-Stokes equations and a much larger time step can be chosen of the order of

$$\Delta t \approx cfl^n \left. \frac{V}{\left| u + c \right| \left| \vec{s}_\xi \right|} \right|^n_{1,J-1} \quad \text{with} \quad cfl^n = cfl^1 2^{\frac{n-1}{4}}$$

Where a 1-D explicit inviscid stability condition, using data at the upper left boundary of the mesh, is used to compute Δt, multiplied by a parameter, cfl^n, which starts at cfl^1 and then doubles during each 4 time steps. Again, this parameter should have a limit to avoid the loss of precision by adding and subtracting large numbers on finite word size computers. Also, Δt should be limited so that a signal should not travel the whole length of the flow field in a single time step. This implies that the above formula should be bounded by at least

$$\Delta t \leq \left. \frac{L}{\left| u_\infty + c_\infty \right|} \right|$$

where L is the length of the flow field and u_∞ and c_∞ are the free stream velocity and speed of sound.

17.9.2.5 Method of Solution of the Implicit Matrix Equations
The set of implicit equations can be solved by Gauss-Seidel Line Relaxation, as discussed in Sec.11.3 in general or Sec.16.5 in particular for flow past a flat plate. Approximate Factorization or the Diagonally Dominant Alternate Direction Implicit (DDADI) methods also discussed in Chapter 11 can be used. For the present problem of flow past a flat plate, with a fine mesh is confined to a thin region along the plate, the Gauss-Seidel Line Relaxation method, the simplest of the three, will suffice.

17.9.2.6 Flat Plate Solutions
Run your program until convergence, about 100 time steps. Start with a low value of the parameter $cfl^1 \approx 0.1$ and increase it each time step as shown above to avoid negative temperatures initially at the plate surface caused by the sudden imposition of the no slip boundary condition on a uniform flow. Limit the growth of this parameter to at most $cfl^n \approx 10$ for the present flat plate case.

Figure 17.12 shows the boundary layer region for laminar flow and Figure 17.13 shows that for turbulent flow using the Baldwin-Lomax turbulence model. The Mach contours for $0.95M_\infty$ are shown in both figures. Note the difference in boundary layer growth rates, laminar with $x^{1/2}$ and turbulent nearly linear growth with $x^{0.8}$. The turbulent boundary layer is seen to be thicker, with fuller velocity profiles, than the laminar boundary layer.
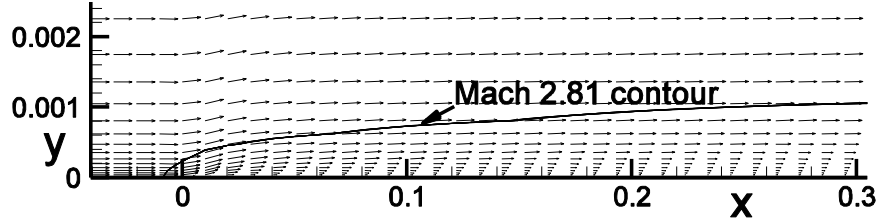
Figure 17.12 Laminar boundary layer formation
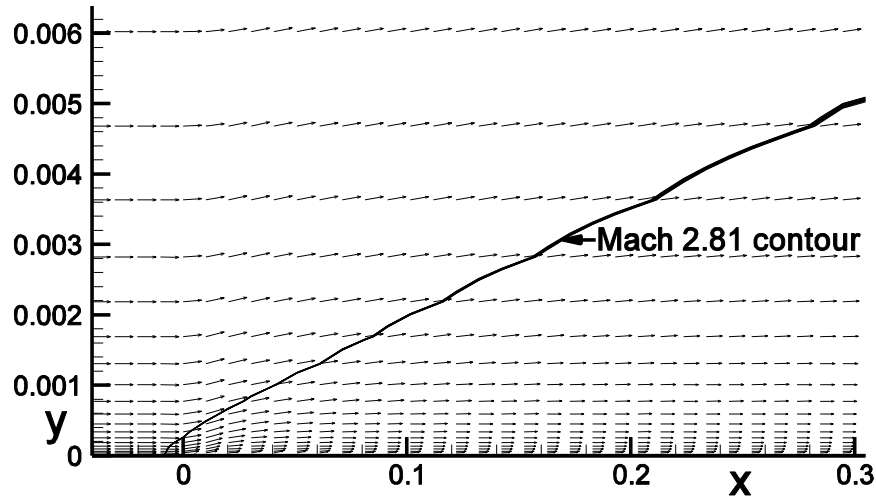
Figure 17.13 Turbulent boundary layer formation

The convergence of the turbulent velocity profiles at $i = I - 2$, near the exit boundary at $x = 0.29m$, are shown in Figure 17.14. The profiles are shown every 12 time steps, $n = 12k, \quad for \quad k = 1, \cdots, 7$.

The vertical axis variable is defined by $\eta = y\sqrt{\dfrac{\rho_\infty u_\infty}{\mu_\infty x}}$ and the horizontal axis by u / u_{edge}, where

$u_{edge} = u_\infty$. Compare the scale of the boundary layer thickness with that shown for a Blasius velocity profile in Figure 16.12. The flow converges fairly quickly within 40 time steps. The velocity profiles calculated by the Thin Layer Navier-Stokes and full Navier-Stokes equations are compared in Figure 17.15. They appear to agree perfectly.
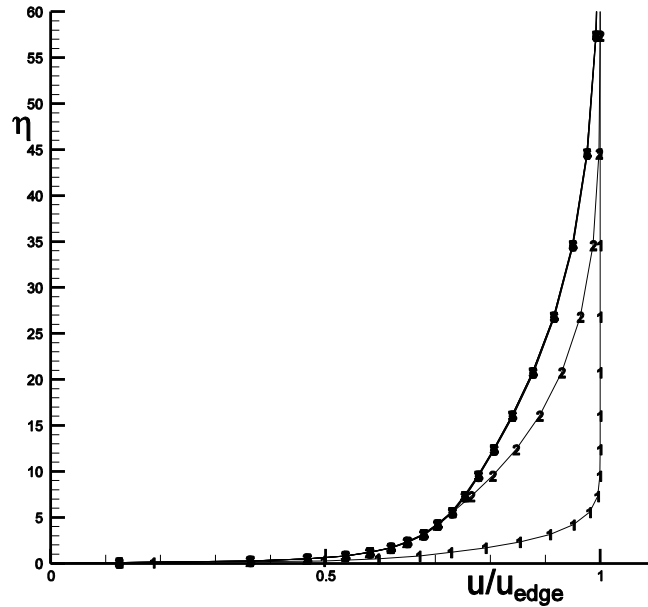
Figure 17.14 Convergence of turbulent velocity profiles
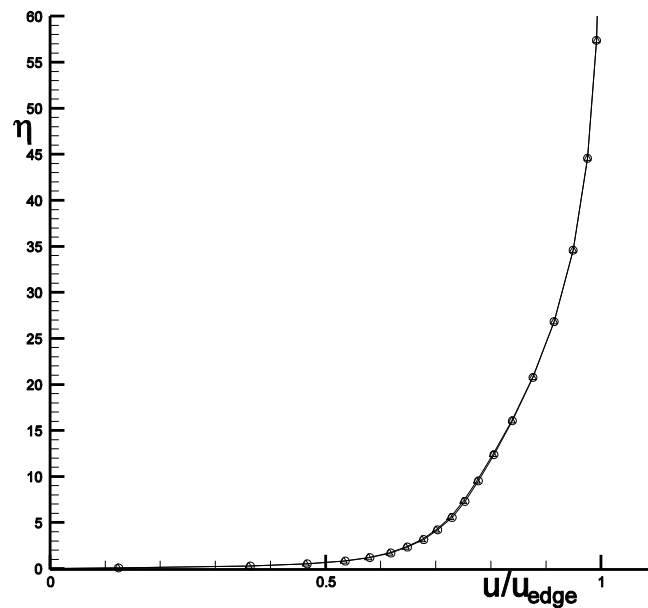
Figure 17.15 Comparison of turbulent velocity profiles,
Full Navier-Stokes and Thin Layer Navier-Stokes

17.9.3 Compression Corner Solution
17.9.3.1 Mesh for the Compression Corner
A 36x32 mesh is shown in Figure 17.16. This mesh, as previously, consists of a fine stretched mesh, containing 20 mesh cells across or 21 points, joined smoothly to an equally spaced outer course mesh, containing 10 more cells to reach the top boundary of the flow field. The mesh point at $i = 2$ is located at $x_2 = 0.883 ft$ ($0.269 m$), near the location of $i = 32$ of the former flat plate

mesh. The corner of the mesh is located at $i_{cnr} = 17$. The mesh is equally spaced in the x direction, with $\Delta x = (L - x_2)/15$. There are 15 interior mesh cells ahead of the corner and 19 aft.
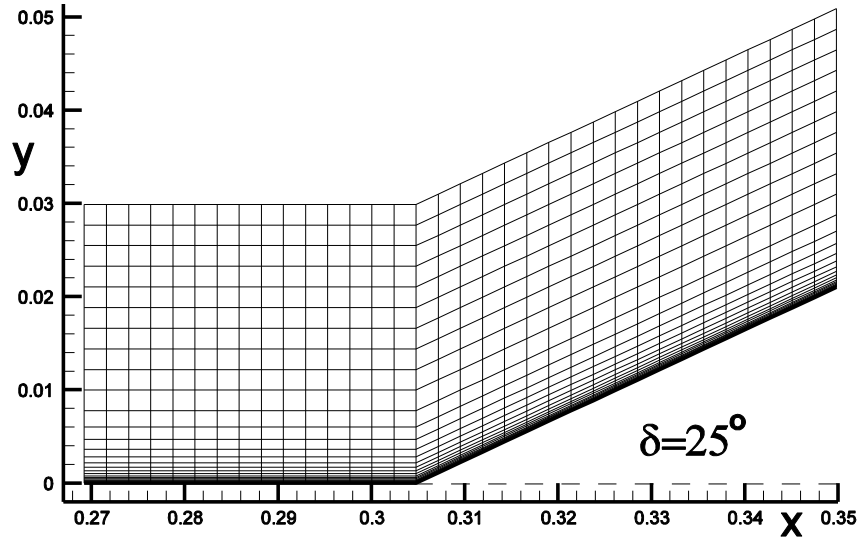
Figure 17.16 Mesh for flow past a flat plate

17.9.3.2 Initial Conditions
The flow variables of column $i = 32$ from the previous flat plate calculation are used to define column $i = 1$ of the present compression corner calculation. These variables include ρ, u, v, T and the eddy viscosity $\varepsilon = \mu_t$. These same variables are used to start the flow downstream of the first column, with the velocity vector turned parallel to the wedge surface within the fine mesh.

$$V_{i,j} = V_{1,j} = \begin{bmatrix} \rho \\ u \\ v \\ T \end{bmatrix}_{1,j} \quad \text{and} \quad \varepsilon_{i,j} = \mu_{t_{i,j}} = \mu_{t_{1,j}}, \quad \text{for all } i \text{ and all } j$$

Correction for or $i \geq i_{cnr}$ and $j < JLFM$, $\quad \begin{array}{l} u_{i,j} = q_{1,j} \cos \delta \\ v_{i,j} = q_{1,j} \sin \delta \end{array} \quad$ where $\quad q_{1,j} = \sqrt{u_{1,j}^2 + v_{1,j}^2}$

The eddy viscosities obtained from the Baldwin-Lomax turbulence model (see Sec.15.7) at $i = 32$ from the flat plate solution are shown below. The FMAX and YMAX values are 196.7m/s and 2.18×10^{-3}m, respectively. The eddy viscosities and laminar viscosity are also compared below. The switching from the inner eddy viscosity to the outer one to determine the turbulent viscosity is shown by the symbols. The values of the turbulent viscosity exceed the laminar values by two orders of magnitude over much of the boundary layer.

23
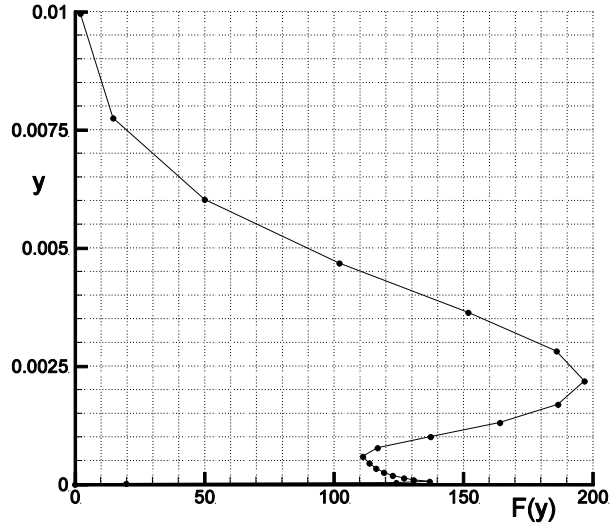
Figure 17.17 Baldwin Lomax plot of F(y) vs. y
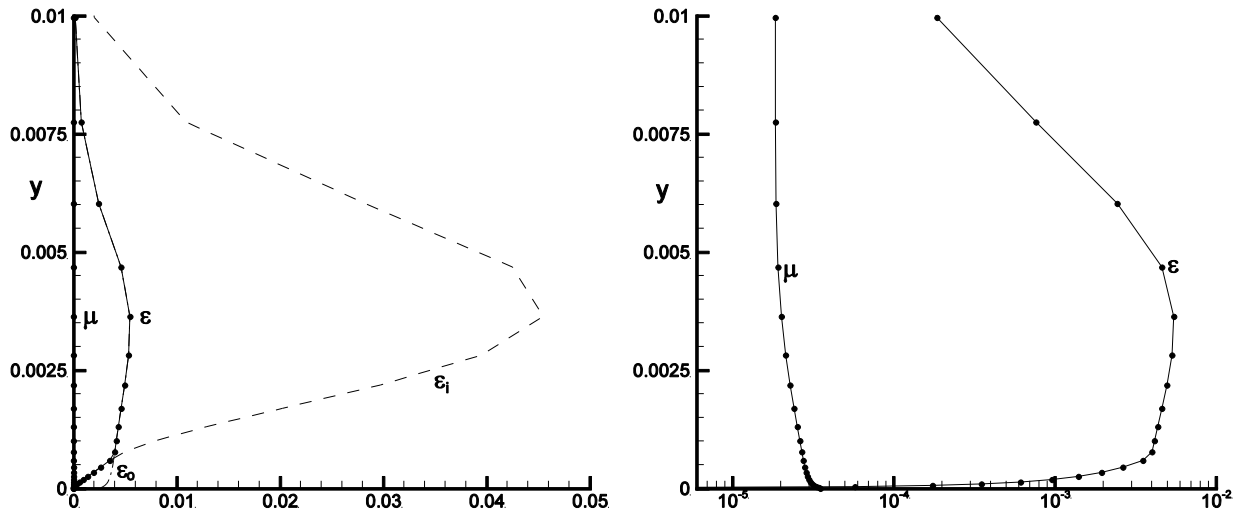
Figure 17.18 Baldwin-Lomax turbulent eddy viscosities $\varepsilon_i, \varepsilon_o$ and $\varepsilon = \mu_t$, log plot with μ at right

17.9.3.3 Relaxation Turbulence Model
Joe Shang modified the algebraic Cebeci-Smith turbulence model to delay the increase in turbulence brought about by the rapid compression as the flow enters the corner region. He considered three possibilities.

    a) <u>Equilibrium Model</u> - uses the model as is, with the calculated eddy viscosity in equilibrium with the local flow variables.

    b) <u>Frozen Model</u> – uses the eddy viscosity values frozen at their upstream values at x_1 ahead of the corner.

    c) <u>Relaxation Model</u> – uses a blend of the local and upstream values depending upon the distance from the upstream location x_1.

24

$$\varepsilon_{i,j} \leftarrow \varepsilon_{1,j} + (\varepsilon_{i,j} - \varepsilon_{1,j})(1 - e^{-\frac{\chi}{10\delta_1}}), \quad where \quad \chi = \begin{cases} 0, & frozen \\ \infty, & equilibrium \\ d_{i,j}, & relaxation \end{cases}$$

and $\quad d_{i,j} = \sqrt{(x_{i,j} - x_{1,j})^2 + (y_{i,j} - y_{1,j})^2}$ and δ_1 is the thickness of the boundary layer at x_1

Use the Baldwin-Lomax turbulence model instead of the Cebeci-Smith model for the present calculations.

17.9.3.4 Boundary Conditions
The conditions at the entrance and top boundaries are again fixed at their initial values. The top boundary will have free stream values. The implicit values for δU vanish along these two boundaries.

Solid wall boundary conditions are used along the lower boundary. Again, along the exit boundary the flow will be supersonic outside the boundary layer and will remain attached within it. The simple shift condition, $U_{I,j}^n = U_{I-1,j}^n$ and $\delta U_{I,j}^n = \delta U_{I-1,j}^n$, should suffice.

17.9.3.5 Method of Solution of the Implicit Matrix Equations
The same solution procedure used for the flat plate can be used here to solve the compression corner flow problem.

17.9.3.6 Compression Corner Solutions
Run your program until convergence, about 100 to 150 time steps. Start with a low value of the parameter $cfl^1 \approx 0.1$ and increase it each time step as before, limiting the growth of this parameter to at most $cfl^n \approx 10$.

Figures 17.19-17.23 compare the results, using the equilibrium and frozen turbulence models, obtained with the Modified Steger-Warming method with first order accuracy. Note the increase in size of the flow separation region for the frozen compared to the equilibrium turbulence model results. The results obtained by experiment (C. H. Law, "Supersonic, Turbulent Boundary-Layer Separation," *AIAA Journal*, Vol. 12, June 1974, pp.794-797) fall in between. Shang noticed the rapid increase in the levels of turbulence within the compression corner region using the equilibrium model, which he believed to be unrealistic. He slowed the rapid response of the calculated eddy viscosity to local conditions using a relaxation procedure and found that this gave excellent agreement with experiment.
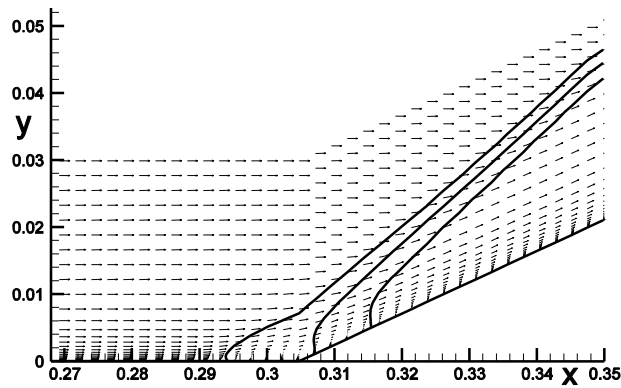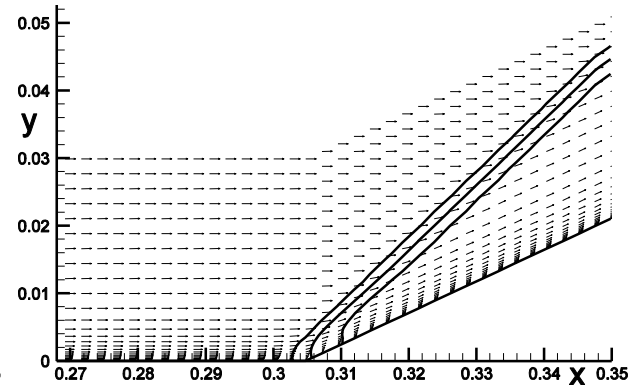
(a) Frozen turbulence model   (b) Equilibrium turbulence model

Figure 17.19 Velocity vectors and pressure contours, 1st order accuracy
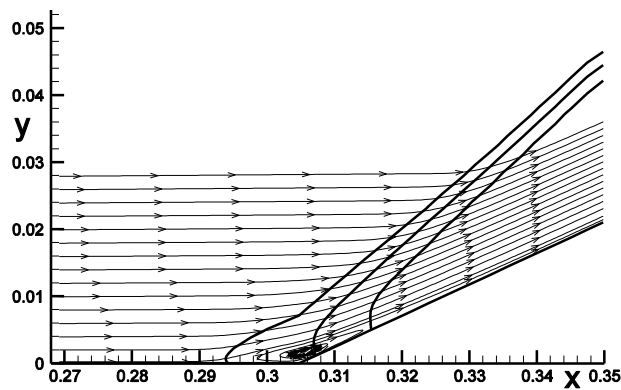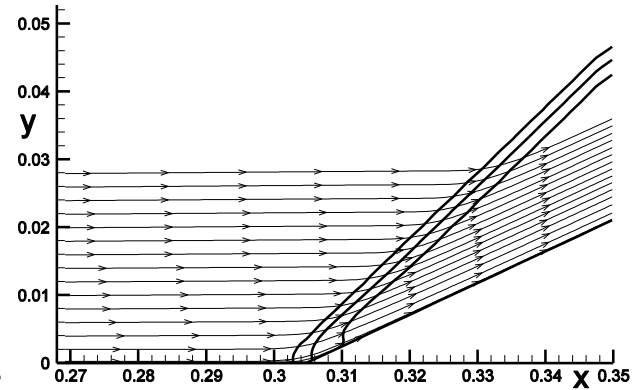
(a) Frozen turbulence model   (b) Equilibrium turbulence model

Figure 17.20 Streamlines and pressure contours, 1st order accuracy
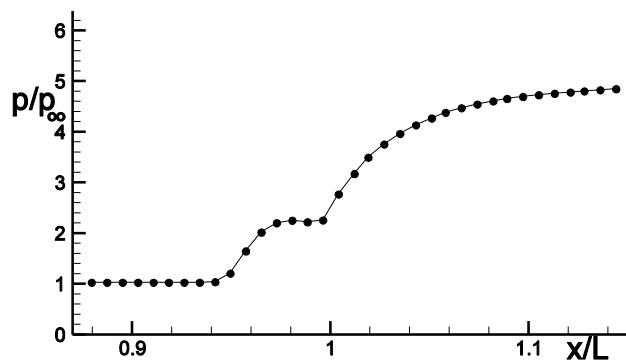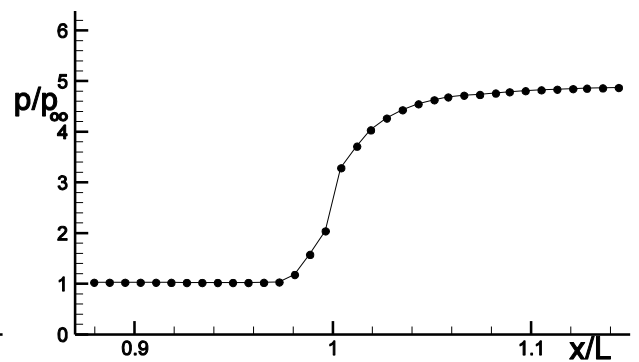
(a) Frozen turbulence model   (b) Equilibrium turbulence model

Figure 17.21 Surface pressure, 1st order accuracy

26
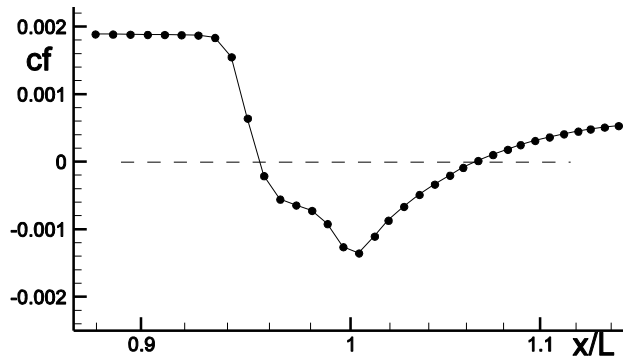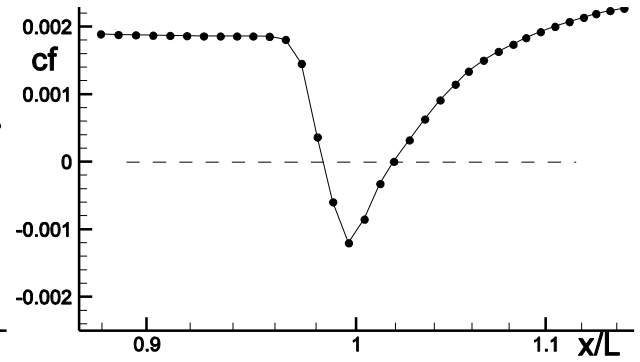
(a) Frozen turbulence model   (b) Equilibrium turbulence model

Figure 17.22 Skin friction, 1st order accuracy
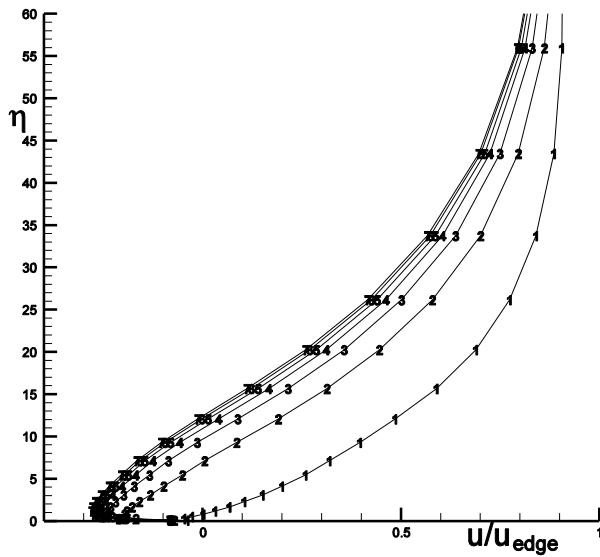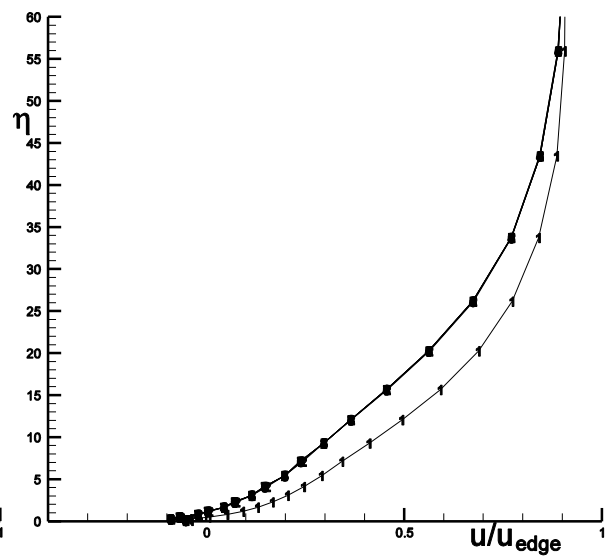
(a) Frozen turbulence model   (b) Equilibrium turbulence model

Figure 17.23 Convergence of velocity profiles at corner, 1st order accuracy

Figures 17.24-17.28 show the results using the relaxation procedure of Shang, calculated with the Modified Steger-Warming method at second order of accuracy.
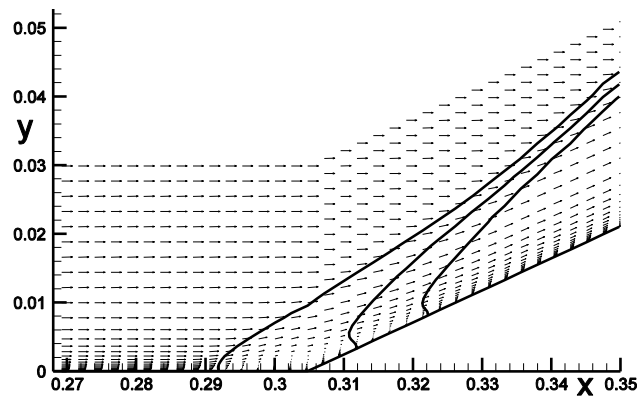
Figure 17.24 Velocity vectors, 2nd order accuracy
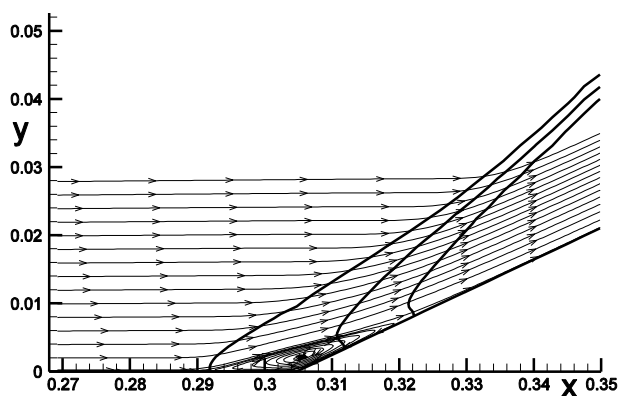
Figure 17.25 Streamlines, 2nd order accuracy

27
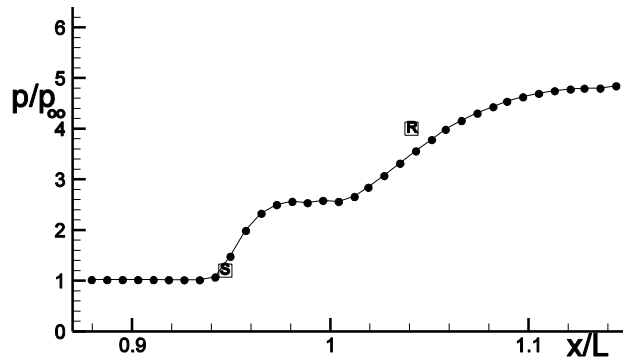
Figure 17.26 Surface pressure, 2nd order accuracy
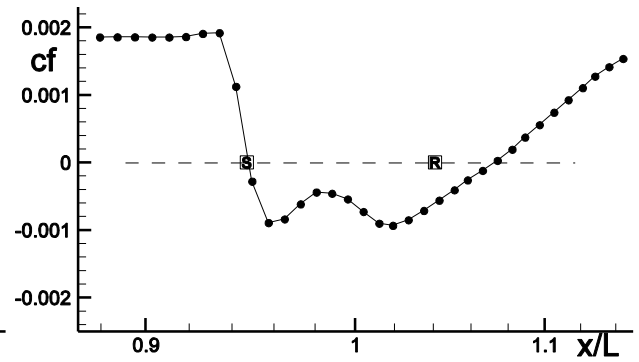
Figure 17.27 Skin friction, 2nd order accuracy
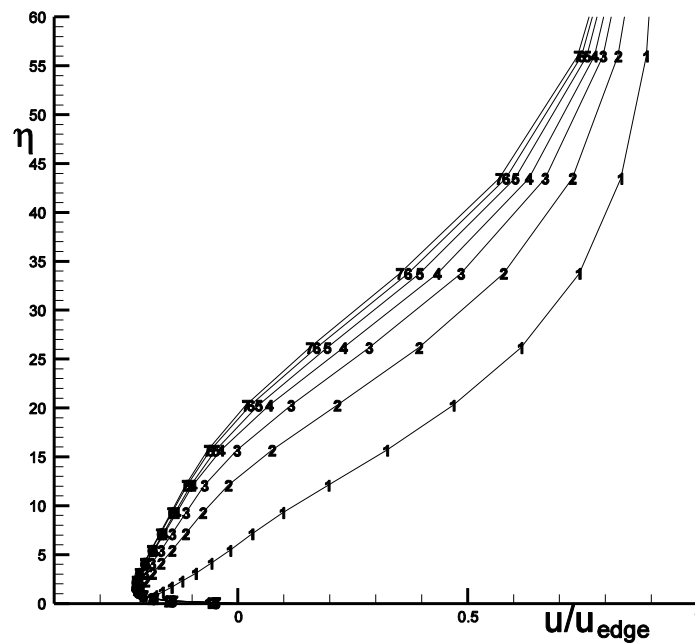
Figure 17.28 Convergence of velocity profiles at corner, 2nd order accuracy

Figures 17.26 shows surface pressure and the location of the experimental separation and reattachment points, taken from the values shown in the figures of Shang's paper. Figure 17.27 compares the location of these points for the present simulation. The separation region along the surface is given by the negative values for skin friction. The agreement is good at separation, but the experiment shows a stronger compression at the reattachment point and consequently a shorter region of separation. Shang's results show better agreement with experiment.

17.10 Application: Viscous Flow Past a Circular Arc Airfoil

17.10.1 Exercise: Solve the Navier-Stokes equations for transonic flow past a circular arc airfoil. Use an implicit method for $M_\infty = 0.908$ flow past a 6% thick circular arc airfoil of chord length $c = 1m$ on a 51×51 mesh, with 21 equi-spaced points over the airfoil and stretched to far field boundaries 50 chord lengths away. Use either the Modified Steger-Warming Flux Vector Split method or the Roe Flux Difference Vector Split method.

Figure 17.28 Mach contours

17.10.2 Solution Approach: Start with 51×51 mesh for inviscid flow governed by the Euler equations. We will add 20 mesh points across the boundary layer region later for solution by the Navier-Stokes equations. The flow has a total pressure and temperature near atmospheric, $p_t = 1.0 \times 10^5 N/m^2$ and $T_t = 300^o K$. The figure below shows a schematic of the flow field. Use the same mesh, initial conditions and boundary conditions as in Sec.14.4.2.

Figure 17.29 Flow volume about symmetric circular arc airfoil

Figure 17.30 Mesh near airfoil for Euler equations

17.10.3 Time Step Size

The time step limit for an explicit method on a an arbitrary mesh for inviscid flow was given in Sec.14.4.1 as

$$\Delta t \leq \min_{i,j} \left\{ \frac{V_{i,j}}{\left|\vec{q}_{i,j} \cdot \vec{S}_{i+1/2}\right| + \left|\vec{q}_{i,j} \cdot \vec{S}_{j+1/2}\right| + c_{i,j}\sqrt{\left|\vec{S}_{i+1/2} \cdot \vec{S}_{i+1/2}\right| + \left|\vec{S}_{j+1/2} \cdot \vec{S}_{j+1/2}\right|}} \right\} = \Delta t_{max}$$

where the velocity $\vec{q} = u\vec{i}_x + v\vec{i}_y$. Calculate Δt_{max}^n each time step and set $\Delta t^n = cfl^n \cdot \Delta t_{max}^n$. Start with a $cfl^0 = 0.9$ and increase it to 10 for an implicit method for solving the Euler equations. Use an approach similar to that discussed in Sec.16.5, i.e. $\Delta t^n \approx cfl^n \Delta t_{max}^n$ with $cfl^n = 2^{\frac{n-1}{4}} cfl^0$.

17.10.4 Solutions

Run your program until convergence, about 120 time steps.

17.10.4.1 Euler Solutions

Initially, $\Delta t_{max}^0 = 0.64 \times 10^{-4} s$ and $\Delta t^0 = 0.58 \times 10^{-4} s$, then Δt^n increased by a factor of 2 each 4 steps. After 16 time steps cfl^n reached and was held to 10. Solutions are shown below.
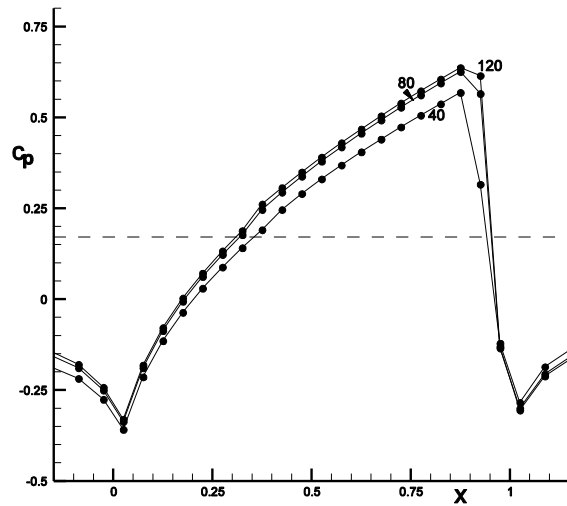
Figure 17.31 Convergence of c_p vs. x, Euler   **Figure 17.32** Mach contours at $n = 120$ steps
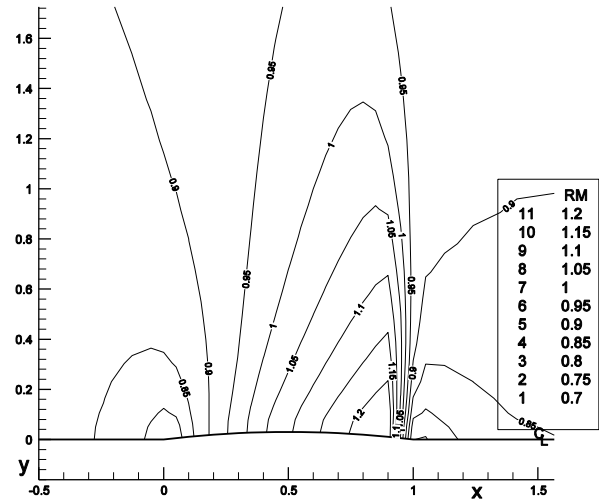
17.10.4.2 Extension of Mesh for Navier-Stokes Equations

The approach used to create a "seamless' joining of a refined mesh across the boundary layer to a coarse mesh for the inviscid part of the flow, described in Sec.16.9.2, will be used here for viscous flow past a circular arc airfoil.

The minimum spacing Δy_{min} in the fine mesh is chosen such that $\Delta y_{min} = \delta(L)/N$, where N is an integer, for example 40, and $\delta(L)$ is an estimate of the boundary layer thickness at a distance L

for the airfoil leading edge, for example $L = c$, the chord length of the airfoil. We can use the formula for a flat plate laminar boundary layer for our estimate $\delta(L) = \dfrac{5L}{\sqrt{\mathrm{Re}_L}}$. The Reynolds number based on chord length is $\mathrm{Re}_c = \dfrac{\rho_\infty u_\infty c}{\mu_\infty} = \dfrac{0.7984 \times 291.3 \times 1}{1.638 \times 10^{-5}} = 1.419 \times 10^7$. The boundary layer thickness $\delta(c) \approx 1.33 \times 10^{-3} m$ and

$$\Delta y_{\min} = \delta(c) / 40 \approx 3.32 \times 10^{-5} m.$$

Consider the mesh ahead of the airfoil. The first mesh point, located on the symmetry line, is denoted by $y_2 = 0$, the next by $y_3 = \Delta y_{\min}$ and the rest by

$$y_j = y_{fm} \frac{e^{\kappa \frac{j-2}{JLFM-2}} - 1}{e^\kappa - 1}$$

where the number of fine mesh points is given by $JLFM = 21$. This equation introduces two unknowns, κ and y_{fm}, the height of the fine mesh. If we take the value Δy_{Euler}, the mesh point spacing of the Euler mesh at the symmetry line, for start of the spacing at y_{fm} into the coarse mesh, such that Δy_{Euler} equals the fine mesh spacing if continued for one more mesh point, we obtain a second equation for κ and y_{fm}.

$$\Delta y_{Euler} = y_{fm} \frac{e^{\kappa \frac{JLFM-1}{JLFM-2}} - 1}{e^\kappa - 1} - y_{fm}$$

We define can rearrange the two equations for solution via Newton's method for vector functions, as follows

$$f_1(\kappa, y_{fm}) = \Delta y_{\min} - y_{fm} \frac{e^{\kappa \frac{1}{JLFM-2}} - 1}{e^\kappa - 1} = 0$$

and

$$f_2(\kappa, y_{fm}) = \Delta y_{Euler} - y_{fm} \frac{e^{\kappa \frac{JLFM-1}{JLFM-2}} - 1}{e^\kappa - 1} + y_{fm} = 0$$

Then

$$A_k (X_{k+1} - X_k) = -F(X_k)$$

where the Jacobian matrix $A = \dfrac{\partial F}{\partial X}$ and the vectors $X = \begin{bmatrix} \kappa \\ y_{fm} \end{bmatrix}$ and $F = \begin{bmatrix} f_1(\kappa, y_{fm}) \\ f_2(\kappa, y_{fm}) \end{bmatrix}$

Starting with $X_1 = \begin{bmatrix} 1 \\ \Delta y_{Euler} \end{bmatrix}$ and using 10 iterations is usually more than sufficient to find values for κ and y_{fm} that satisfy the two equations $f_1(\kappa, y_{fm}) = 0$ and $f_2(\kappa, y_{fm}) = 0$. For the present case $\kappa \to 7.320$ and $y_{fm} \to 0.1066m$, which places about half the fine mesh points within the boundary

layer. The mesh is then continued into the coarse grid in the same manner as earlier for the Euler inviscid mesh, starting at y_{fm} with mesh spacing Δy_{Euler} and covering the distance to 50 chords above the airfoil, using a new $\kappa = 4.569$ solved for via Newton's method. The vertical spacings before the airfoil can be used over the airfoil proportionately to $\dfrac{50c - y_{i,2}}{50c}$. The x spacings are unchanged from the Euler grid. The mesh for the Navier-Stokes equations is shown below.
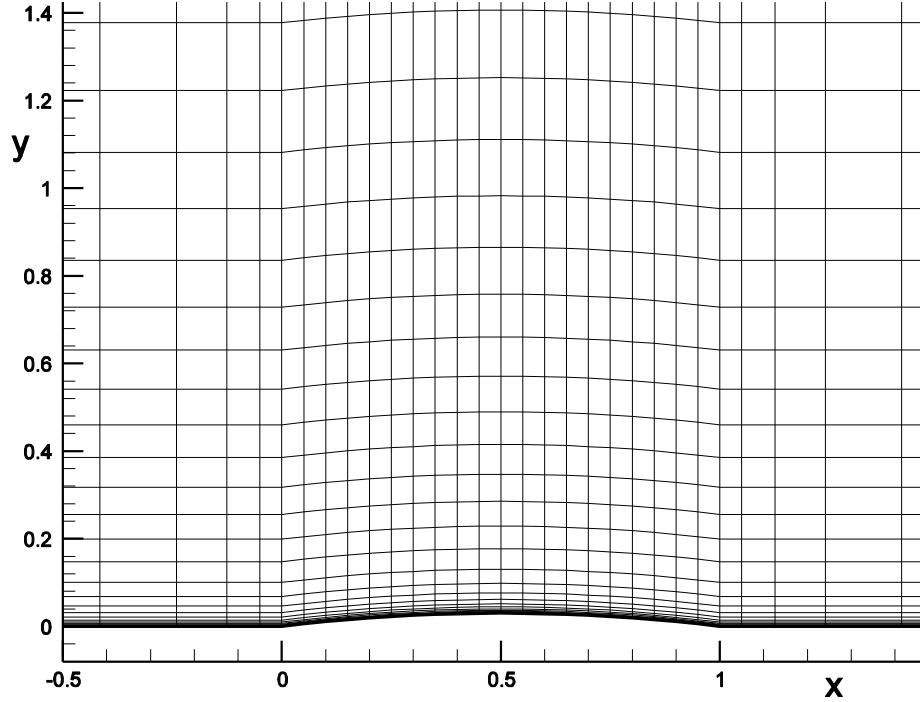
Figure 17.33 Viscous mesh near airfoil for Navier-Stokes equations

17.10.4.3 Time Step Size
The time step limit for an explicit method on a an arbitrary mesh for viscous flow is given below

$$\Delta t \leq \min_{i,j} \left\{ \frac{V_{i,j}}{\begin{array}{c} \left|\vec{q}_{i,j}\cdot\vec{S}_{i+1/2}\right|+\left|\vec{q}_{i,j}\cdot\vec{S}_{j+1/2}\right|+c_{i,j}\sqrt{\left|\vec{S}_{i+1/2}\cdot\vec{S}_{i+1/2}\right|+\left|\vec{S}_{j+1/2}\cdot\vec{S}_{j+1/2}\right|} \cdots \\ \hline \cdots\cdots +2\nu_{i,j}\left(\left|\vec{S}_{i+1/2}\cdot\vec{S}_{i+1/2}\right|+2\left|\vec{S}_{i+1/2}\cdot\vec{S}_{j+1/2}\right|+\left|\vec{S}_{j+1/2}\cdot\vec{S}_{j+1/2}\right|\right)/V_{i,j} \end{array}} \right\} = \Delta t_{max}$$

where the velocity $\vec{q} = u\vec{i}_x + v\vec{i}_y$ and $\nu = \mu/\rho$. Note that the quotient above has been broken because of its length. Compare this formula with Eq.16.3 given in Chapter 16 for a cartesian mesh, where $V = \Delta x\Delta y$, $\vec{S}_i = \Delta y\vec{i}_x$ and $\vec{S}_j = \Delta x\vec{i}_y$. Calculate Δt_{max}^n each time step and set $\Delta t^n = cfl^n \cdot \Delta t_{max}^n$. Start with a $cfl^0 = 0.9$ and increase it to 1000, again increasing cfl^n by a factor of 2 each 4 steps.

32

17.10.4.4 Solutions for Flow Past a 6% Thick Airfoil
Run your program until convergence, about 240 time steps.

17.10.4.4.1 Navier-Stokes Solutions, Laminar Flow
Initially, $\Delta t_{max}^0 = 0.87 \times 10^{-7} s$ and $\Delta t^0 = 0.79 \times 10^{-7} s$, then Δt^n increased by a factor of 2 each 4 steps. After 44 time steps cfl^n reached and was held to 1000. Solutions for laminar flow are shown below.
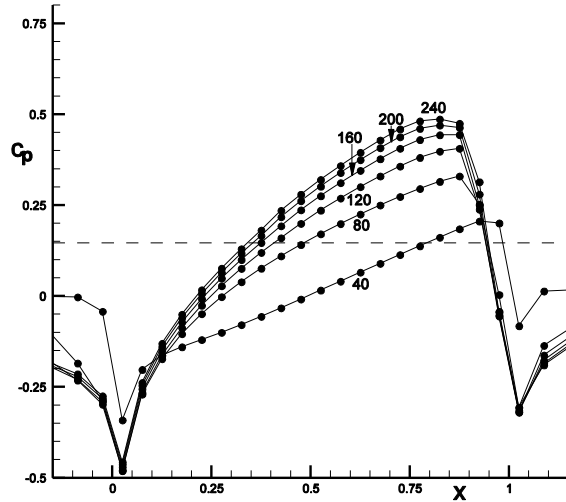
Figure 17.34 Convergence of c_p vs. x, $th/c = .06$
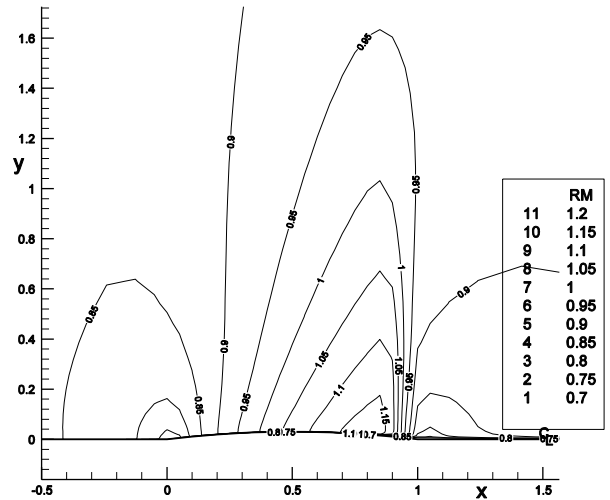
Figure 17.35 Mach contours at $n = 240$ steps
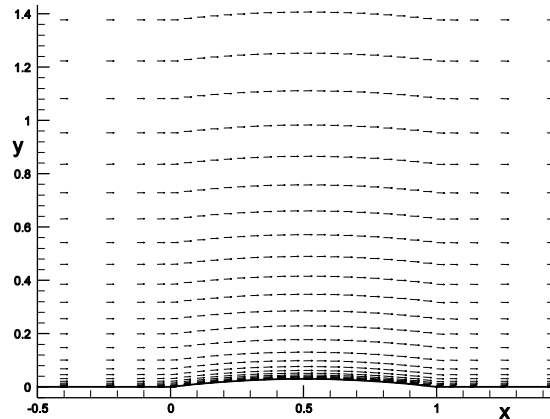
Figure 17.36 Velocity vectors near airfoil
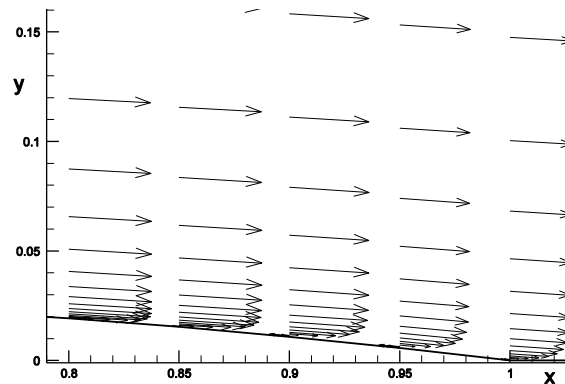
Figure 17.37 Velocity vectors at trailing edge
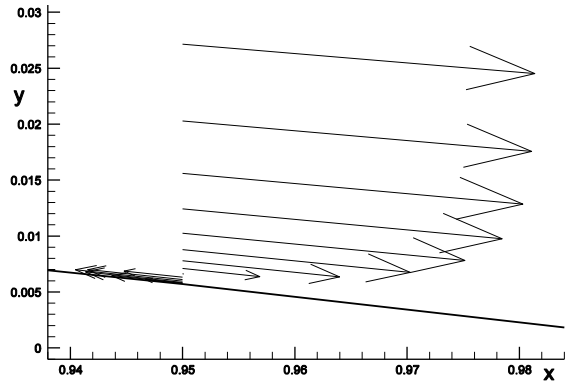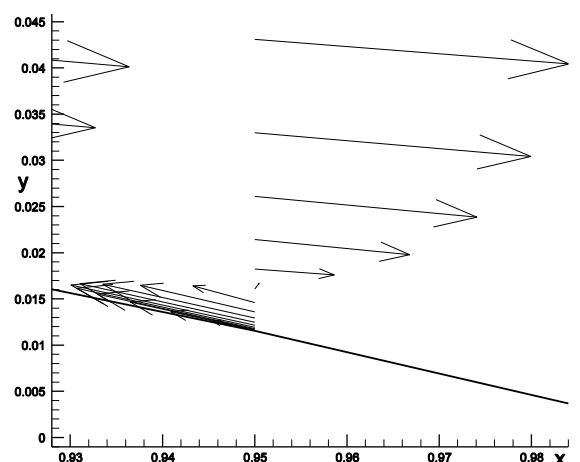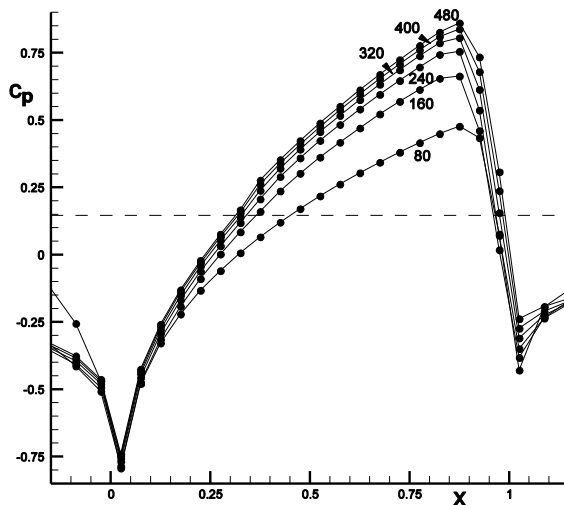
Figure 17.38 Velocity vectors at $x = 0.95m$
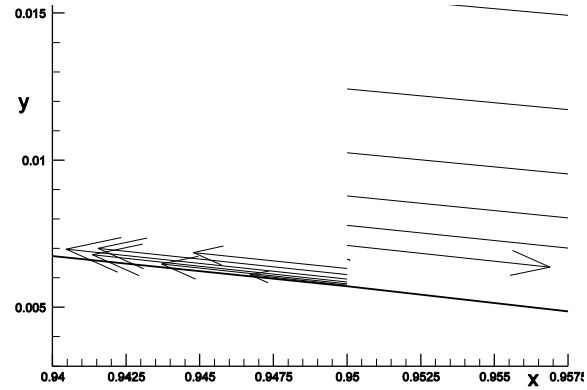
Figure 17.39 Velocity vectors detail at $x = 0.95m$

Notice the reversed flow in the details of the velocity vectors in Figures 17.37-39.

17.10.4.4.2 Navier-Stokes Solutions, Turbulent Flow

Solve the Reynolds-Averaged Navier-Stokes (RANS) equations for turbulent flow using the Baldwin-Lomax turbulence model (see Sec.15.7). Use the same mesh as before for laminar flow. The initial time step sizes were the same as for laminar flow, with cfl^n reaching 1000 in 44 time steps.
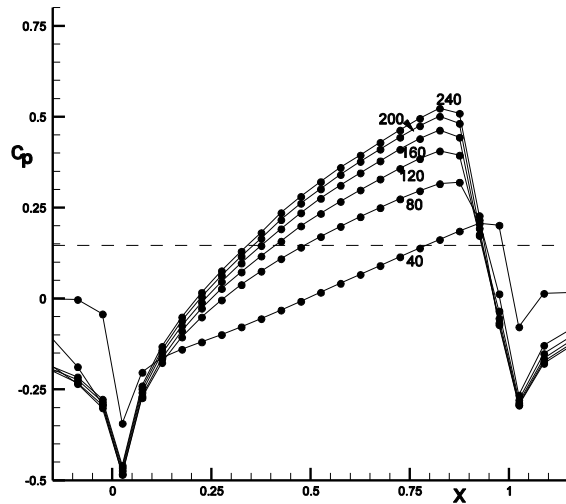
Figure 17.40 Convergence of c_p vs. x, $th/c = .06$
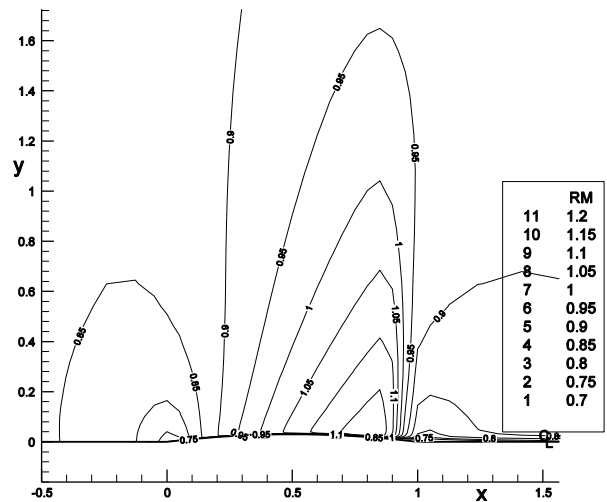
Figure 17.41 Mach contours at $n = 240$ steps

34
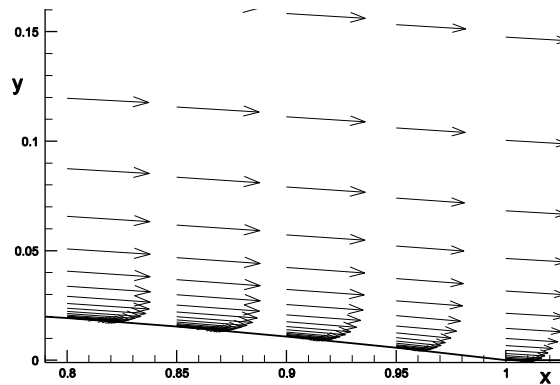
**Figure 17.42** Velocity vectors at trailing edge
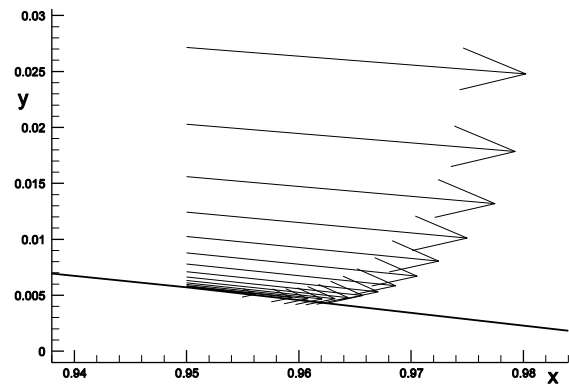
Figure 17.43 Velocity vectors at $x = 0.95m$

Notice the absence of reversed flow in the details of the velocity vectors in Figures 17.43 and 44. The turbulent mixing within the boundary layer brought higher tangential momentum nearer to the airfoil surface so that the flow could pass through the strong shock produced adverse pressure gradient without separation.

17.10.4.5 Solutions for Flow Past a 12% Thick Airfoil

The above cases were rerun for $M_\infty = 0.908$ flow past a 12% thick circular arc airfoil. The cfl^n limit was reduced to 500.

17.10.4.5.1 Navier-Stokes Solutions, Laminar Flow
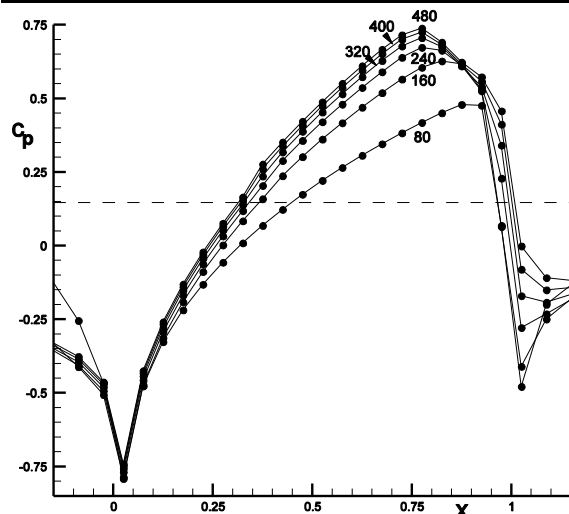
Figure 17.44 Convergence of c_p vs. x, $th/c = .12$
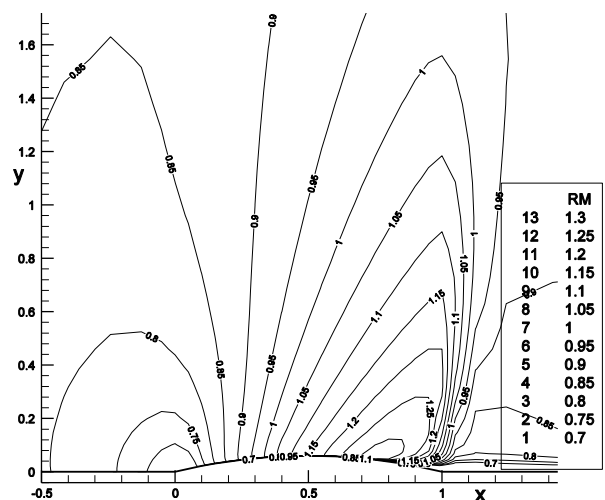
Figure 17.45 Mach contours at $n = 480$ steps

The flow past a 12% thick circular arc airfoil shows in Figure17.47 considerably more separation at the trailing edge for the laminar flow than the 6% thick airfoil.

35
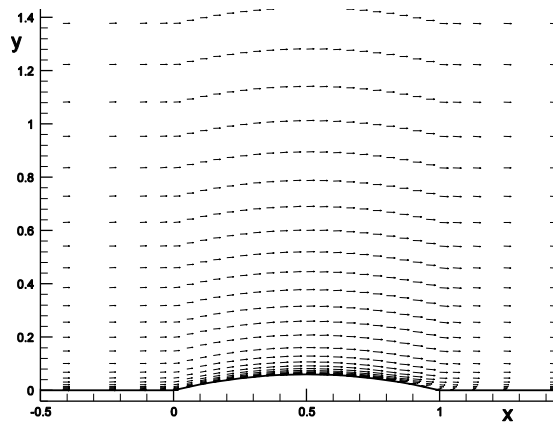
Figure 17.46 Velocity vectors near airfoil
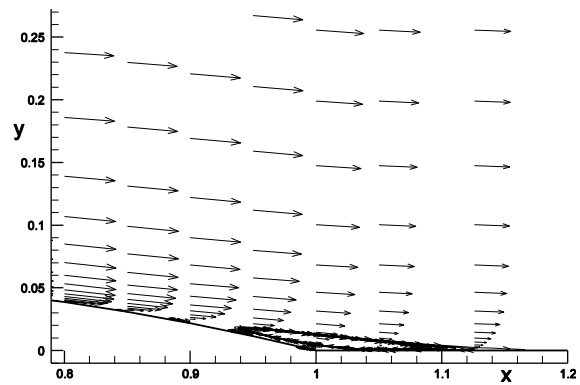
Figure 17.47 Velocity vectors at trailing edge
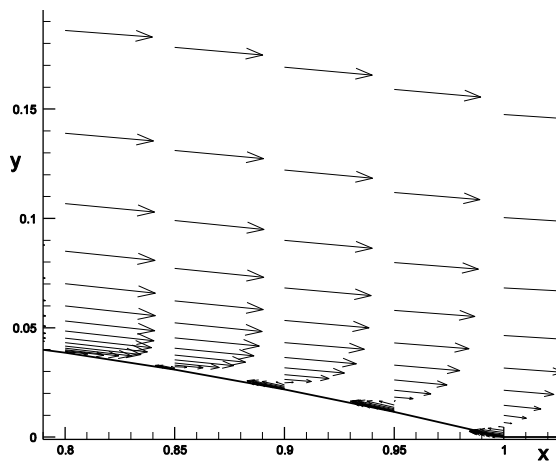
Figure 17.48 Velocity vectors at $x = 0.95m$

Figure 17.49 Velocity vectors detail at $x = 0.95m$

17.10.4.5.2 Navier-Stokes Solutions, Turbulent Flow

Figure 17.50 Convergence of c_p vs. x, $th/c = .12$
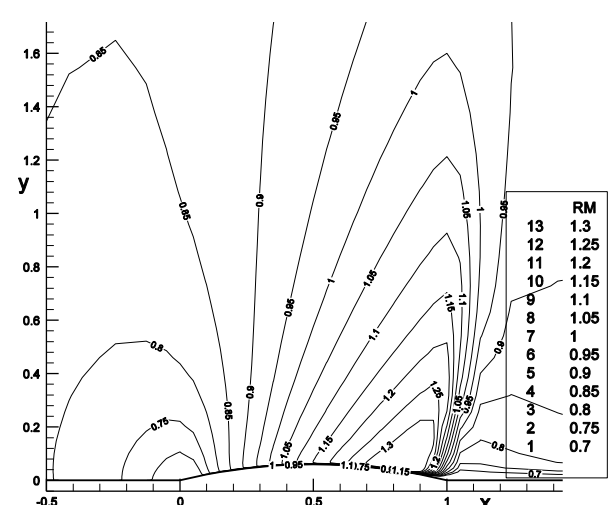
Figure 17.51 Mach contours at $n = 480$ steps

36
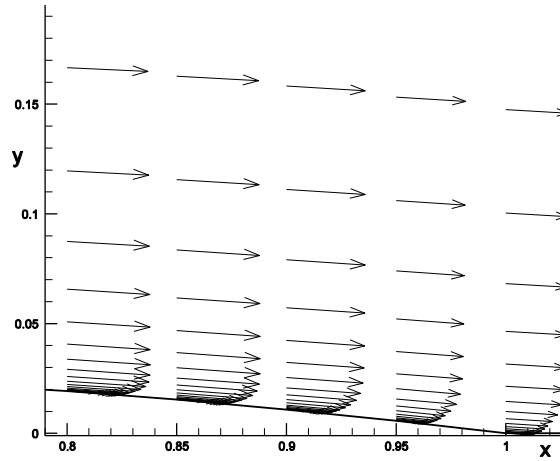
Figure 17.52 Velocity vectors at trailing edge
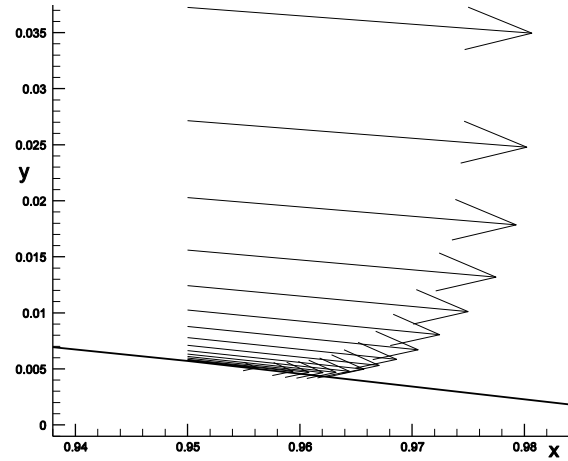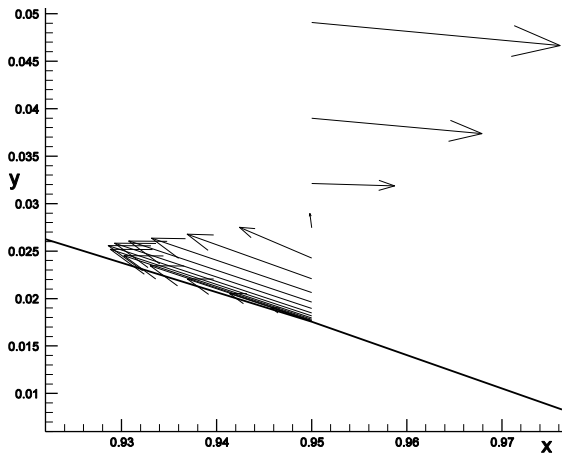

Figure 17.53 Velocity vectors at $x = 0.95m$

Again, turbulence energized the boundary layer, thus preventing separation.

17.10.4.6 Solutions for Flow Past a 18% Thick Airfoil

The above cases were rerun for $M_\infty = 0.908$ flow past a 18% thick circular arc airfoil. The cfl^n limit was 500.

17.10.4.6.1 Navier-Stokes Solutions, Laminar Flow

The separated region is now more pronounced. Note that a plateau has now formed in the c_p distribution in the separation region, similar to those in Figures 16.26, 16.30, 17.21a and 17.26.
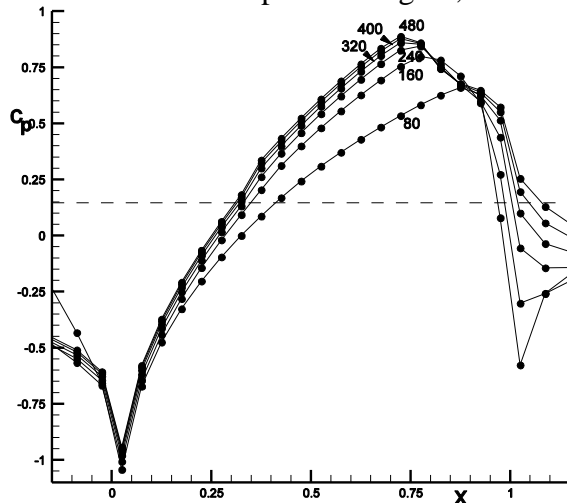
Figure 17.54 Convergence of c_p vs. x, $th/c = .18$
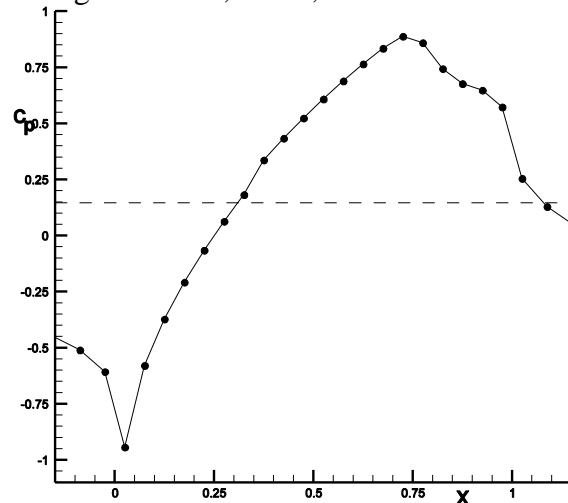
Figure 17.55 Converged c_p vs. x at $n = 480$
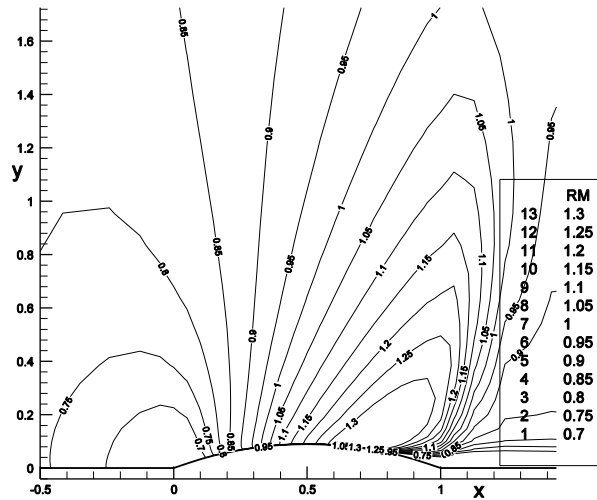
Figure 17.56 Mach contours at $n = 480$ steps
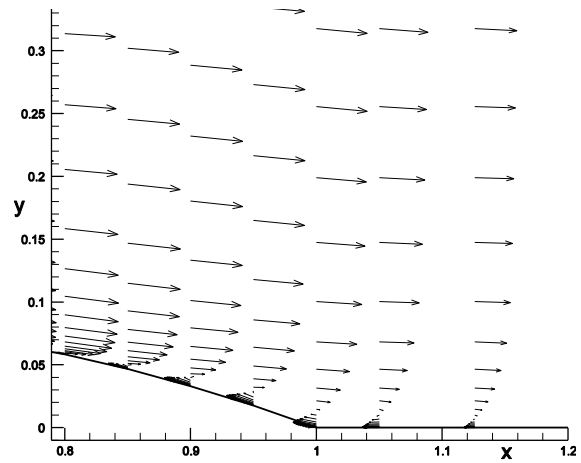
Figure 17.57 Velocity vectors at trailing edge
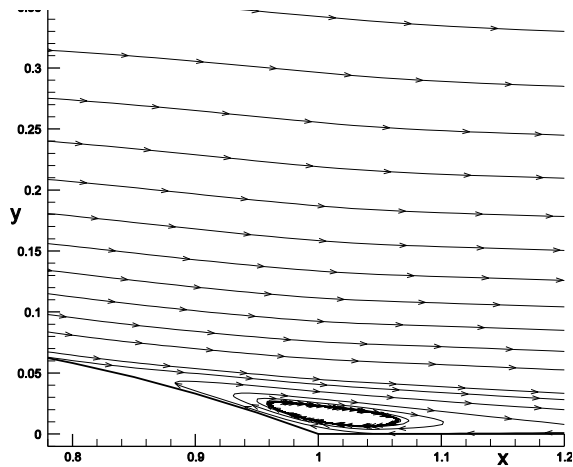
Figure 17.58 Streamlines near trailing edge
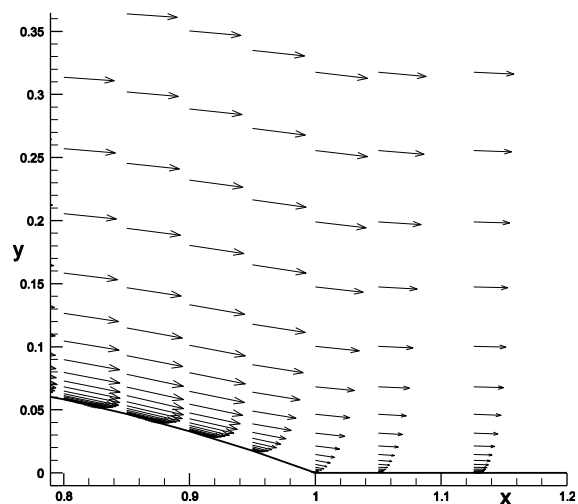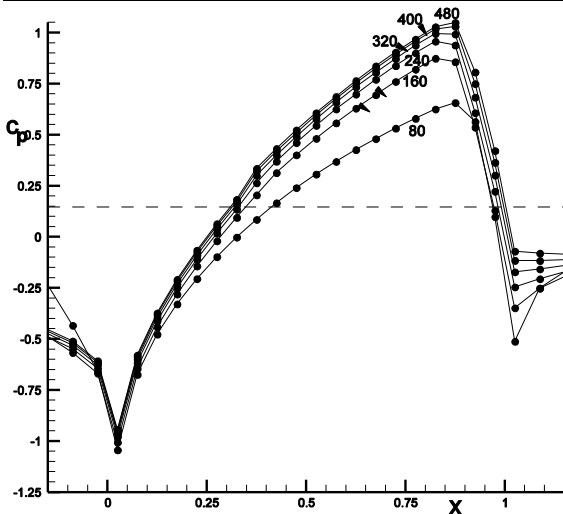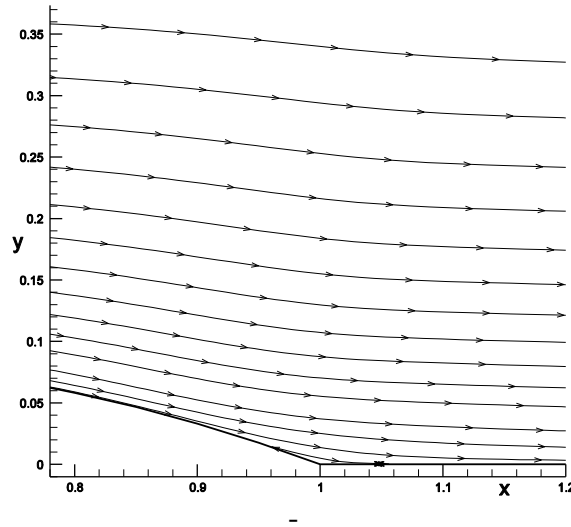

Figure 17.59 Velocity vectors at $x = 0.95m$

### 17.10.4.6.2 Navier-Stokes Solutions, Turbulent Flow

Figure 17.60 Convergence of c_p vs. x, $th/c = .18$ **Figure 17.61** Velocity vectors at trailing edge

Again, turbulence has energized the boundary layer, reducing separation, if any, to a tiny region at the trailing edge, too small to be seen in Figures 17.58 or 59.

+-   **Figure 17.62** Streamlines near trailing edge

Viscous Flow Past a Blunt Body
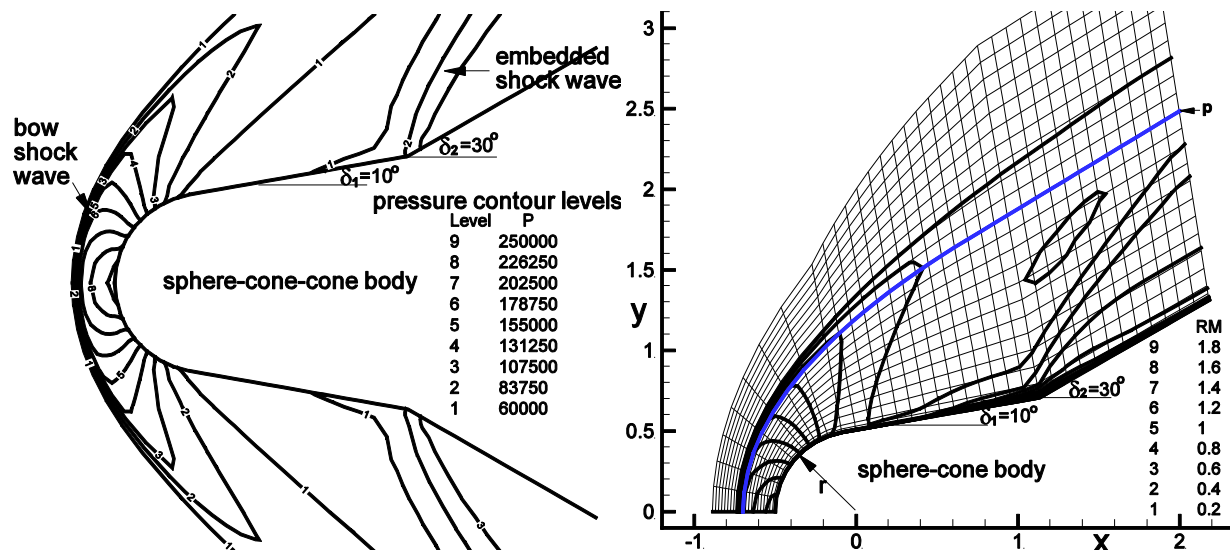
Figure 17.63 Pressure contours, sphere-cone-cone body, and   Mesh with Mach contours

Figure 17.63 shows the pressure contours and mesh for axisymmetric flow past a sphere-cone-cone body. The first half cone angle is $\delta = 10^o$ and the second is $\delta = 30^o$. The radius of the sphere is $r = 0.5m$. The initial sphere-cone part of the geometry is the same as described in part 1 and

second cone starts at the end of the first cone. The freestream pressure and temperature are $p_\infty = 4.563 \times 10^4 \, N/m^2$ and $T_\infty = 300^o \, K$.

Exercise:

Modify your axisymmetric flow program for solving the Euler equations for flow past a sphere-cone body of Sec.14.5.5 to one for solving the Navier-Stokes equations for supersonic flow past a sphere-cone-cone body. Solve the viscous flow equations using the either the Modified-Steger-Warming or Roe methods implicitly.

Mesh

Start with the mesh defined for the sphere-cone body of Sec.14.5.5. The previous mesh had a sphere-cone-junction index $i_{scj} = 10$ and $IL = 24$. We now add 12 additional mesh points along the body with cone-cone-junction index $i_{ccj} = 24$ and IL is now equal to 36. The point spacing along the second cone surface is the same as along the first cone with $\Delta x = r\Delta\theta$. For $i = i_{ccj} + 1 \ to \ IL$

$$x_{i-1/2,2-1/2} = x_{i_{ccj}-1/2,2-1/2} + (i - i_{ccj})\Delta x$$

$$y_{i-1/2,2-1/2} = y_{i_{ccj}-1/2,2-1/2} + (i - i_{ccj})\Delta x \tan \delta_2$$

For the previous mesh $j_{shock} = 10$ and $JL = 20$. We now add 12 mesh points to cover the boundary layer, thus increasing j_{shock} and JL. Now $j_{shock} = 22$, $JL = 32$ and $JLFM = 12$. Compound stretching functions, as discussed in Sec.16.9.2, are used to distribute the points from the body to the shock wave. We choose first to locate the points from the stagnation point to the shock wave along the axis of symmetry, the x-axis, from point $(-r, 0)$ to $(-r - sd, 0)$. The values used for the above results were $(-0.7, 0)$ and $(0, 1.2)$. We also choose the minimum spacing to be $dx_{min} = 10^{-5} r$ to resolve the boundary layer region. Thus, $x_{2-1/2,2-1/2} = -r$ and $x_{2-1/2,3-1/2} = -r - dx_{min}$, where points $x_{2-1/2,j-1/2}$ lie along the axis of symmetry. In the fine boundary layer mesh for $j = 2 \ to \ JLFM$

$$x_{2-1/2,j-1/2} = -r - d_{fm} \frac{e^{\kappa \frac{j-2}{JLFM-2}} - 1}{e^{\kappa} - 1}$$

where d_{fm} is the distance from the stagnation point to the fine mesh limit, to be determined. The spacing of the points from the fine mesh limit to the shock along the axis of symmetry is given by

$$\Delta x_{cm} = \frac{sd - d_{fm}}{J_{shock} - JLFM} \quad \text{and} \quad \text{for} \ j = JLFM + 1 \ to \ JL, \quad x_{2-1/2,j-1/2} = -r - d_{fm} - (j - JLFM)\Delta x_{cm}$$

The two unknowns to be found are κ and d_{fm} and the two functions to be solved via Newton's method are

$$f_1(\kappa, d_{fm}) = \Delta x_{min} - (x_{2-1/2,2-1/2} - x_{2-1/2,3-1/2}) = \Delta x_{min} - d_{fm} \frac{e^{\kappa \frac{1}{JLFM-2}} - 1}{e^{\kappa} - 1} = 0$$

$$f_2(\kappa, d_{fm}) = \frac{sd - d_{fm}}{J_{shock} - JLFM} - \left(d_{fm} \frac{e^{\kappa \frac{JLFM-1}{JLFM-2}} - 1}{e^\kappa - 1} - d_{fm} \right) = 0$$

Values determined for κ and d_{fm} are $\kappa = 8.219$ and $d_{fm} = 1.454 \times 10^{-2} m$.

For the mesh shown in Figure 17.63, the lines $\xi = i - 1/2$ for $i = 2$ to i_{scj} are radial, starting at the origin and making an angle of $\theta_{i-1/2} = (i-2)\Delta\theta$ with respect to the negative x-axis, and those for $i = i_{scj}$ to IL, are at angle $\theta_{i-1/2} = (isc - 2)\Delta\theta$. Each of these lines, at angle $\theta_{i-1/2}$, passes through the body point at $(x_{i-1/2,2-1/2}, y_{i-1/2,2-1/2})$ and intersects the parabola representing the shock wave at $(x_{par_{i-1/2}}, y_{par_{i-1/2}})$. The parabola is shown in Figure 17.63 as the grid line marked **p**. As before for inviscid flow past a sphere-cone body, if the slope of the parabola, $\frac{dy}{dx} = \frac{1}{2ay}$, becomes less than the tangent of the shock wave angle for the first cone, in our Mach 2 case $\theta_{shock} \simeq 31.3^o$, then, instead of the curve for the parabola, a straight line extension with slope $\tan\theta_{shock}$ should be used. This will occur before the exit of the mesh, at about $i = 22$ for the present sphere-cone-cone case. Consideration of only the shock with regard to the first cone is, however, sufficient for the present mesh.

The mesh point locations along the axis of symmetry $(x_{2-1/2, j-1/2}, 0)$ are given above. Those along the other $\xi = i - 1/2$ lines are placed proportionately to those along the axis of symmetry, as follows.

$$\text{Let} \quad \Delta x'_{i-1/2} = x_{par_{i-1/2}} - x_{i-1/2,2-1/2} \quad \text{and} \quad \Delta y'_{i-1/2} = y_{par_{i-1/2}} - y_{i-1/2,2-1/2} \;, \quad \text{for each } i$$

then
$$x_{i-1/2, j-1/2} = x_{i-1/2,2-1/2} + \frac{x_{2-1/2, j-1/2} - x_{2-1/2,2-1/2}}{\Delta x'_{2-1/2}} \Delta x'_{i-1/2}$$
$$y_{i-1/2, j-1/2} = y_{i-1/2,2-1/2} + \frac{x_{2-1/2, j-1/2} - x_{2-1/2,2-1/2}}{\Delta x'_{2-1/2}} \Delta y'_{i-1/2}$$
$$\text{, for } j = 1 \text{ to } JL$$

Initial Conditions
The initial conditions are the same as used earlier for the inviscid sphere-cone problem of Sec.14.5.5.

Boundary Conditions
The boundary conditions used earlier for the inviscid sphere-cone problem are the same for the Euler terms of the present sphere-cone-cone problem. In addition, a no slip condition is needed for the velocities used in the viscous terms at body surface. Consider both adiabatic and isothermal

wall boundary conditions. Try the adiabatic wall case first. For the isothermal wall case let $T_w = 300^o K$.

Time step size

Run your program implicitly until convergence, about 250 time steps. Start with a time step $\Delta t^1 = 2.0 \times 10^{-8}$ and double the step size every 4 steps, $\Delta t^n = 2^{\frac{n-1}{4}} \Delta t^1$, until the limit $\Delta t^n = 10^4 \times \Delta t^1$ is reached. During the total time of the run, $\sum_{n=1}^{250} \Delta t^n$, the freestream will have moved about 18 body lengths. For the Roe method you may need to increase σ_0 used in the entropy correction formula from 1.0 to 2.0.

Sphere-Cone-Cone Solutions

Figures 17.63 − 68 show solutions using the first order accurate Modified-Steger-Warming and Roe methods for Mach 2 flow past the sphere-cone-cone body. The surface of the body was treated as adiabatic. Note the appearance of separated flow in Figures 17.66 - 68.
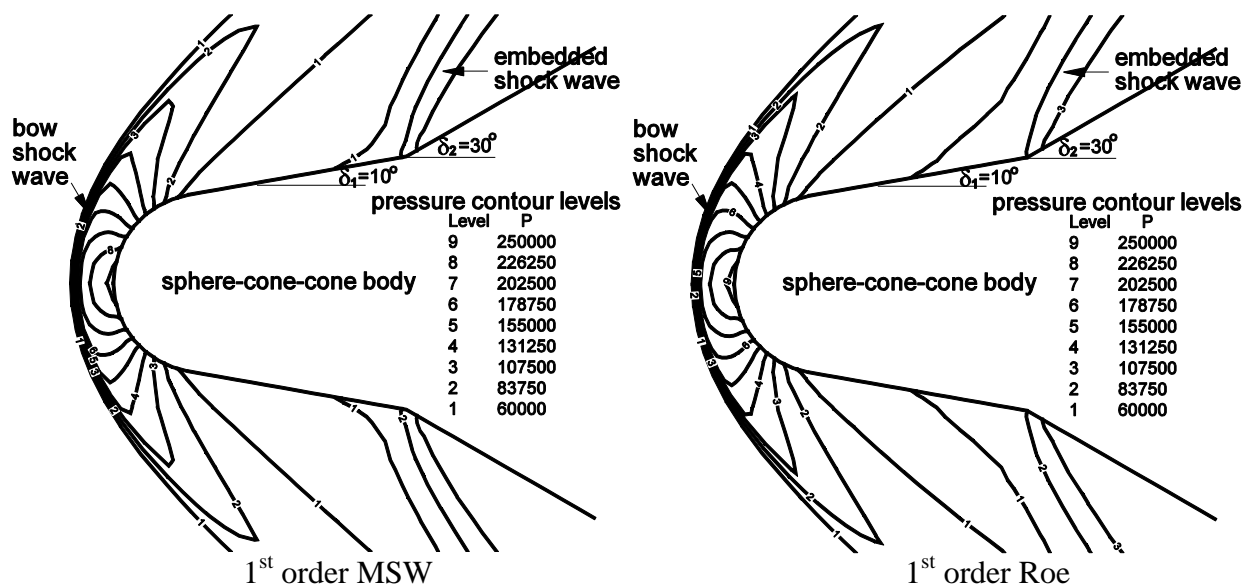
Figure 17.64 Pressure contours, sphere-cone-cone body, adiabatic wall
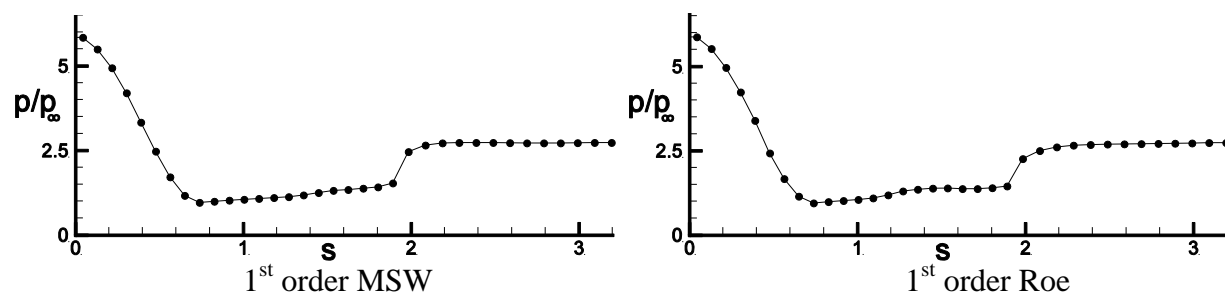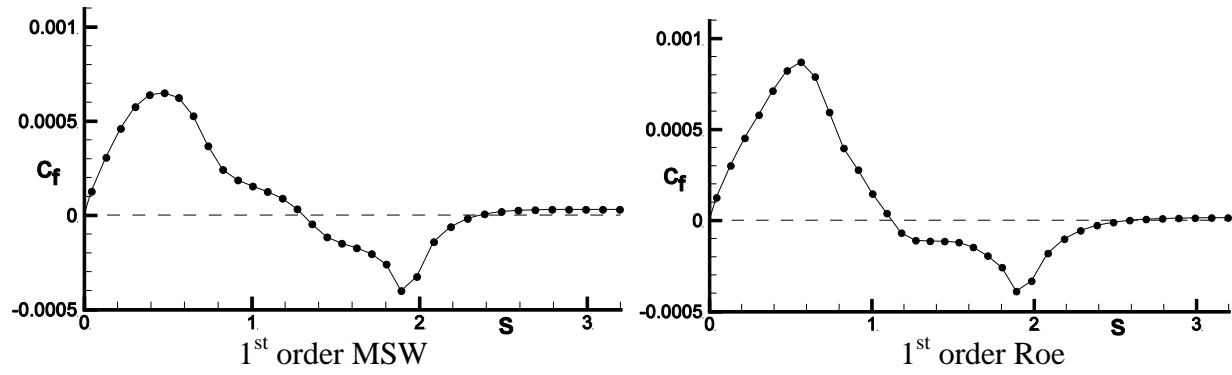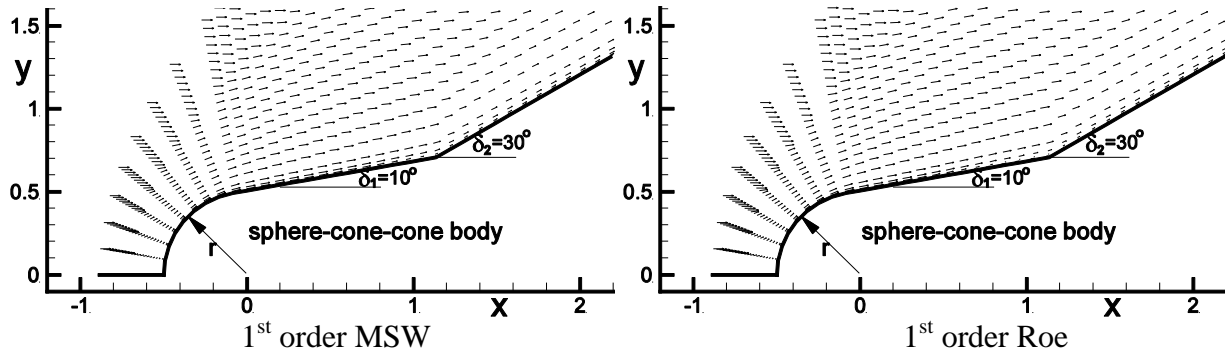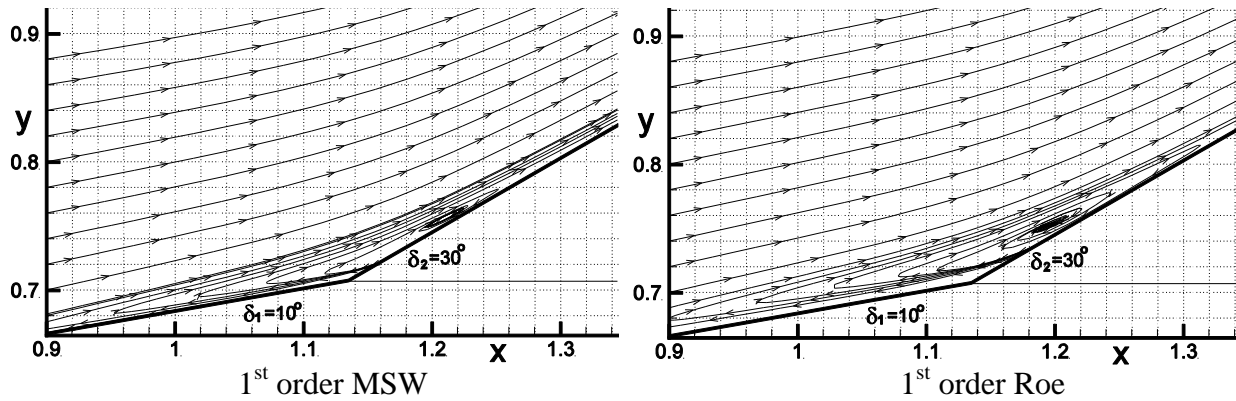

Figure 17.65 Pressure along sphere-cone-cone body surface,
S is distance along the body from stagnation point

Figure 17.66 Skin friction along sphere-cone body surface

Figure 17.67 Velocity vectors

Figure 17.68 Streamlines at cone-cone junction

Figures 17.69 – 72 show second order accurate solutions using the Modified-Steger-Warming algorithm for the isothermal wall case. Note (1) the plateau in surface pressure in the flow separation region, (2) that skin friction increases linearly from the stagnation point and (3) that surface pressure and heat transfer appear as bell shaped curves near the axis of symmetry.

43
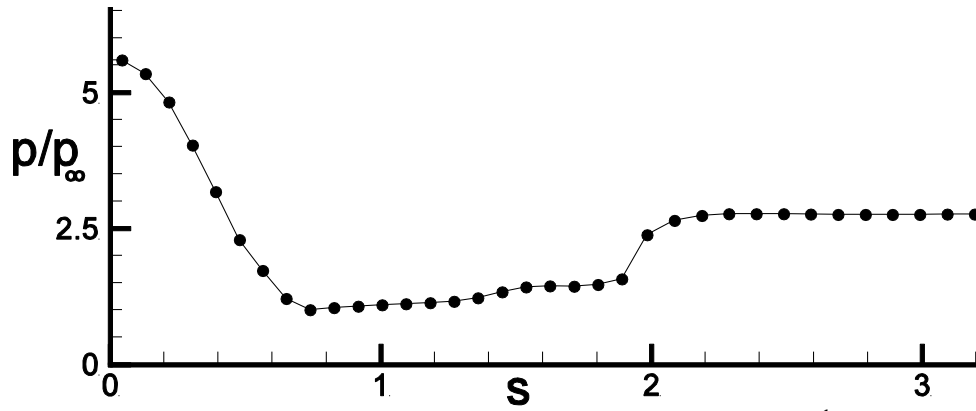
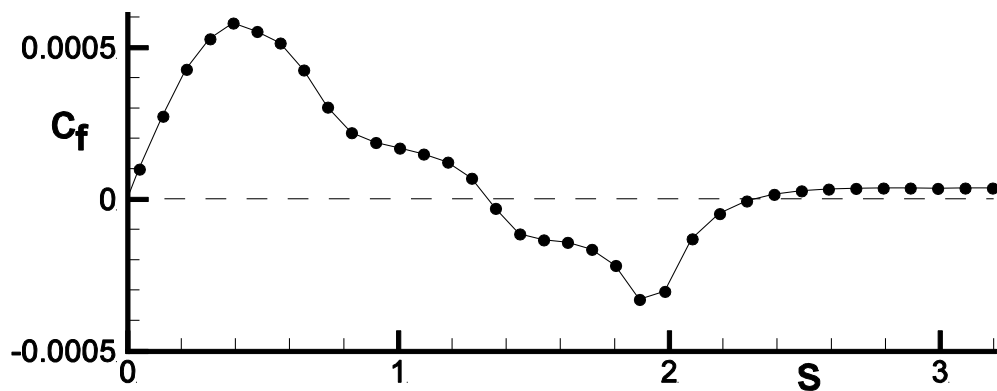**Figure 17.69** Pressure along sphere-cone-cone body surface, 2nd order MSW

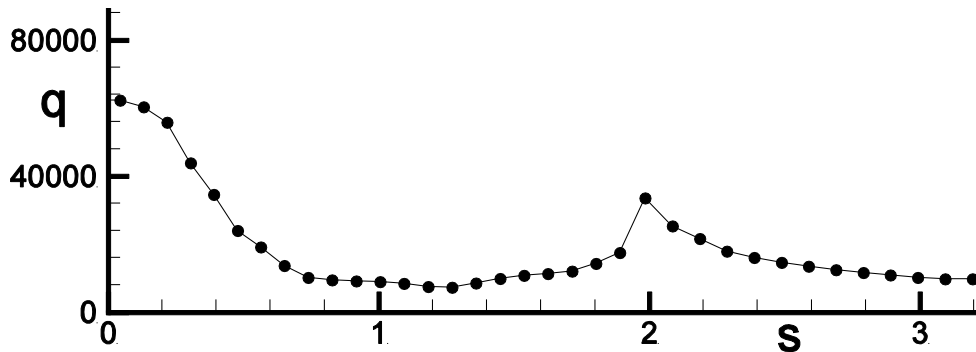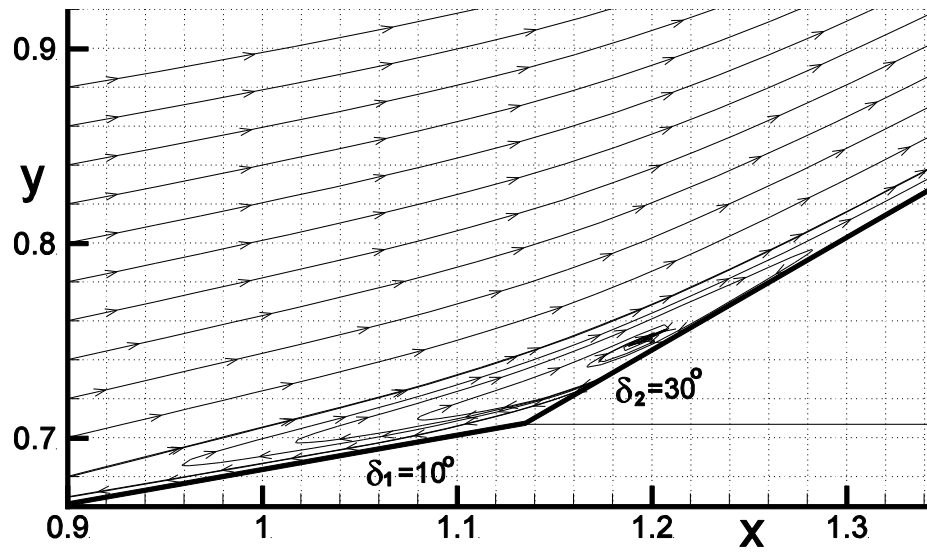**Figure 17.70** Skin friction along sphere-cone body surface, 2nd order MSW

Figure 17.71 Heat transfer along sphere-cone body surface, 2nd order MSW

Figure 17.72 Streamlines at cone-cone junction, 2nd order MSW